Article:
Tetlow, L., Rigby, S.E., Langdon, G.S. et al. (2026) Experimental characterisation of near-field blast loading using digital image correlation on thin plates. International Journal of Impact Engineering, 213. 105671. ISSN: 0734-743X

https://doi.org/10.1016/j.ijimpeng.2026.105671

Experimental characterisation of near-field blast loading using digital image correlation on thin plates

L. Tetlow[1,2], S.E. Rigby[1], G.S. Langdon[1], R.J. Curry[1], G. Pezzola[3]

1. School of Mechanical Aerospace & Civil Engineering, University of Sheffield, UK.

2. Blastech Ltd., Sheffield, UK.

3. U.S. Army Engineer Research and Development Center, Vicksburg, USA

Abstract

Direct measurement of near-field blast loading is seldom in the academic literature, and currently available techniques either produce a small number of discreet temporal measurements, or a single time- and area-integrated value. This limitation is addressed in the current work through the use of stereo high-speed video cameras and Digital Image Correlation (DIC); a technique typically used to determine temporally-resolved, full-field deformation of flexible plates subjected to blast loading. Herein, the focus is on the very first instants of plate response, from which distributions of initial velocity are measured, and – through conservation of momentum – specific impulse is inferred. In total, 29 experiments were performed at 5 different scaled distances covering the entire near-field range (0.17–1.03 m/kg$^{1/3}$). Plate displacements were recorded at 100,000 fps and around 2100 points on the plate surface, effectively enabling full-field measurements of near-field loading distributions, which has previously been unattainable. The results are used to comment on the form and magnitude of blast loading, which ranges from highly centralised, high magnitude loading in the extreme near-field, to relatively uniform, low magnitude loading in the late far-field. The results also show distinct regions of increased localised variability in loading in the mid near-field range, and it is suggested that an idealised, deterministic loading model is not appropriate to capture the true complexity of loading in this region.

Keywords: Blast loading, Near-field, Digital image correlation, Plates

1 Introduction

A major concern of blast protection engineers is to design structures that are robust and provide adequate protection against explosive events. To do this an understanding of the loading they must withstand is required, not only in terms of magnitude but also the spatial distribution as well as inherent variability.

The near-field is when the explosively generated blast wave is in contact with the detonation product cloud (DPC). Hopkinson-Cranz scaling of stand-off distance with the cube-root of explosive mass can be used to compare between different explosive tests. The near-field itself is attributed to a scaled distances of less than 2 m/kg$^{1/3}$ by Tyas (2019). Interactions between the blast wave and the DPC mean that the loading is subject to turbulent structures and instabilities present in the complex fluid dynamic environment (Rigby et al. 2019a, Balakrishnan et al. 2010). Studies have also shown central localisation of specific impulse (Rigby et al. 2019a). These effects mean that near-field loading is spatially variable and subject to regions of localisation. Loading characterisation must therefore not only provide accurate measurements of the specific impulse imparted to a target but also record data points at a sufficiently high spatial resolution. An understanding of how the spatial distribution of loading varies with scaled-distance across the near-field is not currently present within the literature which this article aims to address.

If currently available CFD and FEA modelling codes are to account for near-field loading variability, they require experimental data that captures the complex real-world effects. The accuracy of existing predictors of blast loading such as ConWep and Kingery & Bulmash (1984) predictive charts in the near-field (Z<0.4 m/kg$^{1/3}$) have been questioned by some studies due to a reduced quantity of validating experimental data at this range (Bogosian et al. 2002, Shin et al. 2015). It is evident that testing and characterisation of near-field blast loading in terms of its magnitude, spatial distribution and variability is required, including how these parameters vary with scaled distance.

1.1 Direct measurement of blast loading

The extreme nature of near-field blast loading, with respect to its magnitude and time duration alongside the high temperatures generated means that direct measurement of impulse and pressure is difficult. Piezo-resistive pressure gauges have been demonstrated as a consistent method of assessing blast load parameters within the far-field (Farrimond et al. 2022, Draganić et al. 2018). However, they are unable to withstand the higher pressures and temperatures present at closer scaled distances, whilst the shorter load duration makes them susceptible to resonance within the sensor or limited transient resolution of the recording.

Hopkinson pressure bars (Hopkinson 1914) have been demonstrated as a means of measuring high magnitude pressures and have been used to investigate explosive loading in multiple studies (Cloete & Nurick 2016, Edwards et al. 1992, Taylor et al. 2010). Clarke et al. (2014) used the Characterisation of Blast Loading (CoBL) apparatus, featuring 17 hopkinson pressure bars mounted within a rigid reflecting plate, as a means of determining air and soil-blast pressure time histories at each bar location. Barr et al. (2023) presented a similar experimental arrangement with an increased number of hopkinson pressure bars (33 bars) to characterise extreme near-field loading. This was shown to capture blast

pressures in a similar manner to the CoBL apparatus although was less susceptible to stress wave dispersion within the bars due to a smaller diameter resulting in a higher sensitivity. Qi et al. (2024) demonstrated the use of expansion tube structures deformation characteristics as a means of determining the energy imparted and therefore the power of an explosion. This showcases the use of structural response as a means of inferring blast load parameters, however is still limited to discrete measurement points.

Denefeld et al. (2017) used momentum transfer to free masses as a means of determining specific impulse distributions when investigating the effects of buried charges. A series of concentric rings of equal mass were used to measure the momentum imparted by the loading. This was equated to the impulse applied and Denefeld et al. (2017) used this to establish specific impulse distributions. Similarly to the CoBL apparatus this provides accurate assessment of blast loading distribution however, it is limited in its number of data points. The ring masses will effectively average the loading over its exposed area. This means the method will not effectively record small localisations or variability in loading.

The direct measurement of specific impulse profiles has demonstrated that near-field loading is subject to spatial variation (Rigby et al. 2019a,b, 2020). Tyas (2019) noted that at intermediate scaled distances ($0.5 - 2$ m/kg$^{1/3}$) the CoBL arrangement found local variations in specific impulse at discrete bar locations corroborated by the experimental studies of Clarke et al. (2014) and Rigby et al. (2019a). However, as the measurements are limited to a few discrete data points, the resolution of loading information is too sparse to fully describe the magnitude, size, shape and density of these localisations or their variability. If protection structures are to be designed without knowledge of these loading features they are at risk of localised tearing and fragmentation (particularly if material strength is not homogenous or connections present weak points in the structure) which would render their protective capabilities insufficient. This means experimental characterisation of near-field blast variabilities with data at a high spatial resolution is required to ensure any assessment of variability is sufficiently rigorous.

1.2 Determining loading distributions through optical methods

The complexity of measuring near-field blast directly as well as its sparse dataset has motivated the development of non-intrusive optical methods that can appraise experimental blast loading. Kaufmann et al. (2023) performed pressure reconstruction on steel plates loaded within the shock tube apparatus first described by Aune et al. (2016) and compared against pressure transducer recordings. Deflectometry was used to record curvatures and accelerations across the plate as it deformed during the test. Kaufmann et al. (2023) utilised these values within the virtual field method to determine full-field pressure histories across the plate. Whilst this study demonstrates the practical application and benefits of non-intrusive full field optical assessment of blast loading it is only applicable to small elastic deformations and relies on thin plate theory assumptions. This makes it

less suitable to near-field measurement where thin plates experience large deformations (Wierzbicki & Nurick 1996).

Quinn et al. (2023) also utilises optical methods to determine full-field blast loading data but through the use of pressure sensitive paint (PSP). In their tests a rigid surface was painted with PSP and was recorded by a high speed video camera whilst the specimen was loaded by a small air blast tube. PSP reacts to the oxygen concentration (influenced by air pressure) by changing its degree of luminescence and the camera is able to measure these changes with appropriate filters. Quinn et al. (2023) was able to measure pressure-time histories that compared well with pressure transducer data. They also noted that the full-field nature of the results gives a truer estimation of impulse across a surface when considering localised pressure values compared to pressure transducers at discrete points. Quinn et al. (2023) discusses the limitations of PSP as the paint used within their tests was constrained to pressures of 0-200 kPa. Despite it being able to measure higher values this could come at the expense of accuracy. Another practical complication of these tests was the risk of over-exposing the high speed video camera from luminescence of the explosive fireball.

Kaufmann et al. (2023) and Quinn et al. (2023) both demonstrate the significant benefits of full-field loading data that can be derived from optical measurement techniques. However, their methods both present challenges when applied within the near-field due to the high magnitudes involved. In this case, pressures will exceed the capacity of PSP and the deformations of a given target plate is unlikely to only experience small elastic deformations if thin plate assumptions are to be valid.

1.3 Digital image correlation of blast loaded plates

Digital image correlation (DIC) (Parks 1980) is an optical method commonly used to determine full field displacement data for a specimen painted with a speckle pattern. This was expanded to 3D applications, utilising stereo camera systems able to determine out of plane displacements (Sutton et al. 1983, 1986). Early attempts to apply DIC to blast loaded plates showed resolution and speed at which the camera systems recorded to be a barrier to assessing full field transient displacement behaviour (Fourney et al. 2005, Tiwari et al. 2009).

Aune et al. (2016) utilised 3D DIC at a frame rate of 21 kfps on steel and aluminium plates loaded by a spherical C4 charge. A range of scaled distances between 0.69-1.50 m/kg$^{1/3}$ were tested to assess transient deformation and failure modes of the plate whilst a piezo-electric pressure transducer was used to determine pressure and impulse applied to the structure. This approach was extended by Elveli et al. (2023) to include fragmentation combined with the blast wave to assess more complex loading scenarios. Both studies demonstrated DIC as a method highly suited to investigating structural response to complex blast loading however, DIC was not used as a means of calculating applied loading and was instead measured by the pressure transducer instru-

mentation. Curry & Langdon (2017) used 3D DIC to observe the deformation of a circular blast loaded plate. This was at a faster frame rate than Aune et al. (2016) of 30 kfps but was limited to a central strip along the structure.

Rigby et al. (2019a) used high speed DIC of plates loaded by spherical and cylindrical charges to record full-field structural response at 30 kfps. They were also able to infer specific impulse by extracting the initial velocity of the plate from the DIC results. These values compared well with direct load measurements performed on the CoBL apparatus. The relatively slow speed that the DIC recordings were captured at means that temporal resolution was low and therefore susceptible to inaccurate sampling of initial velocity.

Curry et al. (2025) investigated square blast loaded plates at a far higher speed of 100 kfps and performed a rigorous assessment of error within the DIC post-processing algorithm and optical data. Curry et al. (2025) showed that the faster frame rate reveals further detail of the plate's uptake in velocity and found that inferred specific impulse determined using the methodology of Rigby et al. (2019a) can be affected by structural features and shear wave migration across the target plate. However, Curry et al. (2025) was able to demonstrate that the DIC inferred specific impulse profiles showed excellent agreement with direct measurements (using the CoBL apparatus) data performed at the same scaled distance. The study suggests that DIC instrumentation of a blast loaded plate is a feasible means of characterising loading. However, the effects of structural features and understanding of what is a result of loading solely and not influenced by the structure's response should be investigated across a larger scaled distance range than what was investigated by Curry et al. (2025) ($Z<0.162$ m/kg$^{1/3}$).

The study presented herein comprises an experimental characterisation of near-field blast loading at six discrete scaled distances of 0.17-1.03 m/kg$^{1/3}$. The DIC blast testing methods are used to perform 29 tests of blast loaded plates. Experimental application of high speed DIC has been tuned (through the use of plate thickness, camera system parameters and data processing) to characterise loading across a large range of scaled distances. The results showcase the spatial distribution of near-field blast loading across a surface in a level of detail that is only achievable through full-field optical measurement. The tested range of scaled distances exhibit the evolution of loading distribution from highly localised to near-uniform. Furthermore, the high density of data points and repeat testing establishes a basis for determining near-field loading variability arising from complex interactions between the shock wave and detonation product cloud.

2 Experimental setup

2.1 Plate and clamp frame

The experimental tests comprised a series of thin square target plates subjected to blast loading from a close proximity explosive charge. The test plates were square 1 mm or 3 mm thick 1050-H14 Aluminium clamped between 2 mild steel clamping frames of thickness

25 mm with an exposed area of 300×300 mm. The plate and clamp frame were affixed to a large steel frame using 20 M12 mild steel bolts placed around the plate periphery. The material properties of the plate are shown in Table 1. The measured face of the plate (opposite to the loaded surface) was painted with a speckle pattern to be used as a part of the DIC instrumentation and post-processing.

Table 1: Material properties for Aluminium 1050-H14 (ASM Handbook Committee 1990).

Aluminium 1050-H14 Material Properties			
Density	ρ	2,705	kg/m^3
Poisson's Ratio	ν	0.33	-
Young's Modulus	E	69.0	GPa
Shear Modulus	G	26.0	GPa

2.2 Explosive Charge

The explosive charges were 25 g PE10 near-perfect spheres, shaped within a 3D printed spherical split charge mould and compacted to a consistent density of 1.56 g/cm^3. Euronel 2 non-electronic detonators (EPC Groupe 2022) (equivalent TNT mass of 0.8 g) were used to initiate detonation and placed centrally into the charge, normal to the loaded plate face. Positioning of the charge and detonator was achieved using a polystyrene structure that is illustrated in Figure 1).

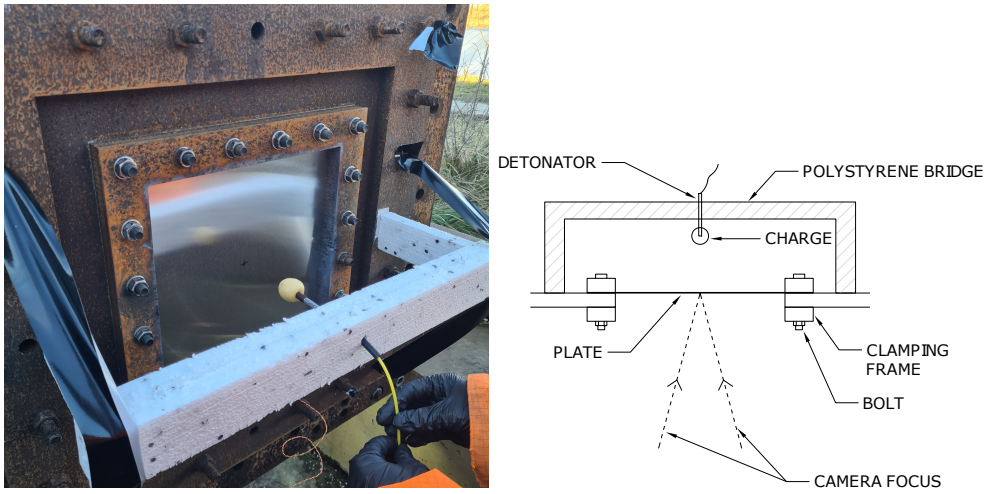

Figure 1: Illustration of charge placement and Polystyrene bridge used during testing.

Charge placement and accurate stand-off was achieved using a Polystyrene bridge structure (see Figures 1) selected designed to limit reflections and interference with the

blast wave. A detonator hole was drilled through the central section of the bridge using a drill press to ensure the detonator was aligned normal to the plate face. The bridge structure was fixed in place by adhesive tape attached to the mounting frame.

2.3 High speed video instrumentation

Each test utilised high speed video (HSV) instrumentation, and the resultant data is used within a DIC post-processing procedure. A stereo pair of Photron Fastcam SA-Z high speed video cameras were focused upon the speckle patterned face of the plate (opposite to the loaded face), with an internal angle of 30° between them, symmetrical about the plate centre. A lateral distance of 2.2 m between the back of the cameras and plate was maintained. Refer to Figure 2 for an illustration of the camera and plate layout.

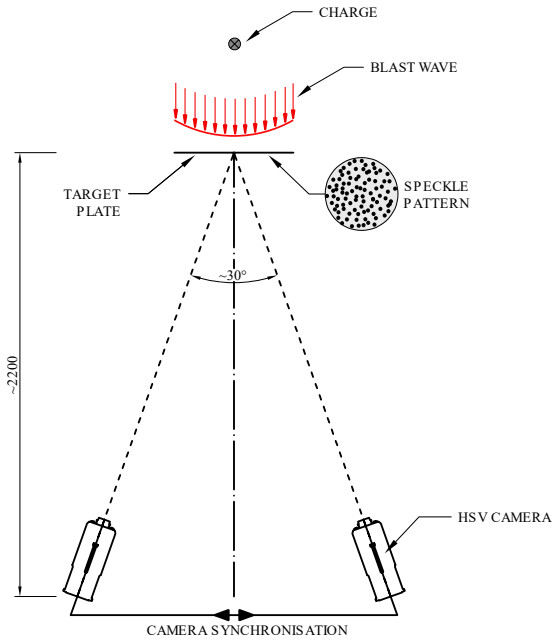

Figure 2: Illustration of HSV camera arrangement.

Both cameras used a Nikon 50 mm lens running at a frame rate of 100,000 fps, a resolution of 640×280 and an aperture of f/4 . Shutter speed was varied between tests to maximise lighting conditions. Both cameras were operated and synchronised using VIC Snap software (Correlated Solutions 2024) and were triggered using a break-wire, fixed to the detonator. A 40 frame (0.4 ms) pre-trigger was used to ensure that the entire detonation and relevant plate response was recorded (a maximum of 10,000 frames).

2.4 Test shot list

Five discrete stand-off distances between the charge and target plate were tested. These were selected to occupy a large portion of the near-field range (scaled distances of 0.171 - 1.026 m/kg$^{1/3}$) and chart the evolution of blast load behaviour throughout. Six individual test groupings, each describing a different configuration of stand-off distance and plate thickness (t), were performed.

The full set of test parameters is summarised in Table 2.

Table 2: Summary of tests performed including stand-off distance (SOD), scaled distance (Z) and plate thickness (t) parameters. Plate material is Aluminium 1050-H14 for all tests.

Group	**Test Ref.**	**SOD** mm	**Z** m/kg$^{1/3}$	**t** mm
A	1-4	50	0.171	3
B	5-9	100	0.342	3
C	10-14	100	0.342	1
D	15-19	150	0.513	1
E	20-24	239	0.817	1
F	25-29	300	1.026	1

3 Digital image correlation

3.1 Speckle pattern and subset

DIC processing was used to determine full-field position, displacement and velocity data across the area of interest on the plate. A vital element of this method is a speckle pattern applied to the target plate which allows the algorithm to differentiate regions across the field of view. The area of interest on the specimen is divided into a series of subsets, which describes a square area of pixels that are spaced at a centre-to-centre value, referred to as step size. Each subset must contain a sufficiently unique portion of the speckle pattern to allow correlation between the frames of the two individual cameras. The algorithm is able to determine where a subset moves from one frame to another based on a similarity score between the subsets. It trials multiple locations and selects the subset with the minimum error function (Curry et al. 2025). Insufficient variation and density in the speckle pattern or too small a subset results in greater potential for error (Kujawińska et al. 2011, Reu & Miller 2008). This error manifests as an inability for the algorithm to accurately match

subsets between frames. A larger subset reduces the spatial resolution of the recording and increases the area over which information is averaged.

As DIC is able to determine movement of a subset throughout the recorded period it can also evaluate its 3D coordinates with time. This requires a series of calibration images that are taken using a specified calibration pattern within the frame of interest. The calibration determines parameters within the algorithm that allow it to calculate the distances and displacements involved with the subset movement during the test. Additionally, the 3D velocities can be computed using the recording frame rate. Small-scale charges were selected for this study to mitigate the shock-wave changing the camera positions during the test which is a potential source of error within the DIC algorithm.

The first 200 frames of the synchronised HSV recordings were processed through the DIC algorithm in the software VIC 3D (Correlated Solutions 2024). The recorded face was painted with a high contrast random 2.5 mm speckle pattern applied using an ink roller, resulting in speckles of approximately 5 pixels in width. A subset size of 17 pixels and a step size of 7 pixels was selected for these tests and a total of 20 images were used for calibration. This process results in full-field transient displacement and velocity equating to approximately 2100 spatial data distributed over the plate surface points per test. Each individual data point represents a full transient description of displacement and velocity throughout the test.

3.2 Error

To assess the base level of error within the DIC results, the 40 frame pre-trigger region was analysed (i.e. the first 0.39 ms across all tests). This time period is prior to the detonation of the charge, therefore no loading is acting on the plate resulting in zero displacement and velocity. Once this period is processed through the DIC algorithm, the magnitude of displacement and velocity deviation from zero can be determined. This was used to assess the base processing error in the DIC methodology.

A total of 81900 displacement and 79800 velocity noise measurements were recorded per test and the data distributions are presented as histograms in Figure 3. Average errors across all data points were calculated as 3.1×10^{-5} mm for displacement data and 0.29×10^{-5} m/s for velocity. The standard deviations were computed as 0.0077 mm 0.40 m/s and Figure 3 demonstrate a half-normal distribution centred close to zero, with a small spread of data. It is concluded that the error is sufficiently small so as to not affect the validity of the results presented herein.

3.3 Extracting specific impulse

The DIC algorithm directly outputs displacement and velocity for each subset and at each given frame throughout the measured period. This provides a realistic representation of how the plate behaves relative to the load, including evidence of localisations and

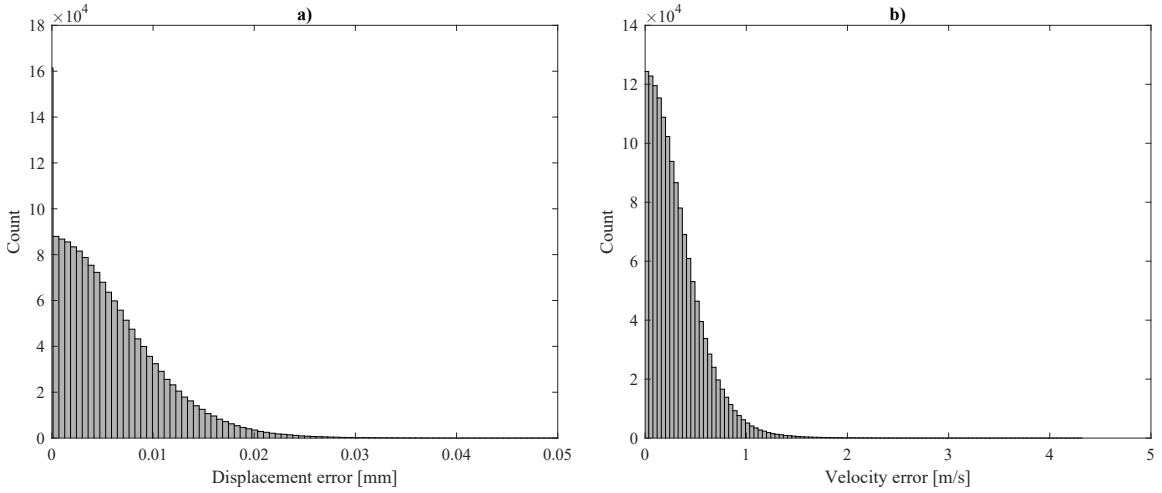

Figure 3: Histograms plotting the distribution of error values for (a) displacement and (b) velocity calculated as the deviation from zero for every data point during the pre-trigger region.

variability within the shock loading. However, the aim of this study is to characterise loading distribution at a high resolution.

To characterise the spatial specific impulse distribution from each test, an adapted version of the methodology presented by Rigby et al. (2019a) is used. This requires the peak velocity resultant from the loading to be sampled from the velocity-time history. This velocity value is then used in conjunction with the plate's 2D spatial density (i.e. density per square metre) to calculate momentum uptake which is equivalent to the specific impulse applied to the plate. The approach is represented by Equation 1 which extends the approach of Rigby et al. (2019a), by considering the entire x-y plane as opposed to a single line splice along the plate's central axes.

$$i(x, y) = \rho t v_{peak}(x, y) \tag{1}$$

Where i is the specific impulse at position (x, y) on the plate; ρ is the plate material density (2705 kg/m^3); t is the plate thickness; v is the maximum velocity measured at the DIC subset of position (x, y).

This methodology relies on some assumptions and simplifications as described below:

(i) The plate is rationalised into a series of discrete masses which are assumed to move freely of one another and as such there is no shear resistance between them. This assumption means that all energy imparted to the plate by the blast wave loading is converted completely to kinetic energy at the moment it impinges upon the plate. No strain energy is produced from shear transfer and each mass behaves as a rigid body. This rationalisation was first presented by Pope (2002) and Tyas & Pope (2003),

then utilised by Rigby et al. (2019b) to simplify spatially variable specific impulse distributions into upper bound energy equivalent uniform impulse distributions. This rationalisation is illustrated by Figure 4.

(ii) Loading from the blast wave is impulsive such that the duration of loading (t_d) is significantly smaller than the time period (T) of the structure (ratio, t_d/T is near-zero). This means that velocity uptake of the plate is assumed to be instantaneous and therefore the peak velocity occurs immediately and is purely a function of the loading, not the structure's response.

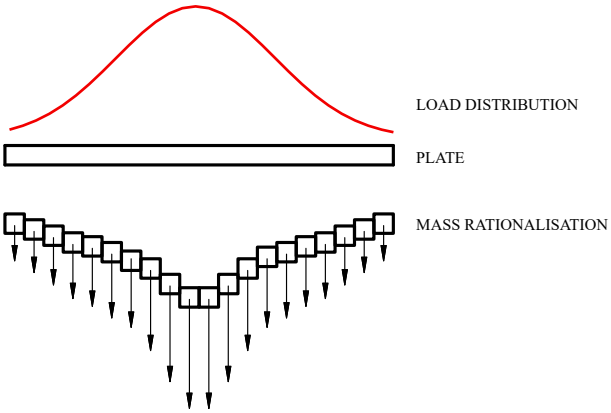

Figure 4: Illustration of the discrete mass rationalisation of the plate (Pope 2002, Tyas & Pope 2003, Rigby et al. 2019a).

(iii) Dissipation of the load through the plate thickness is neglected. The DIC setup used in the experiments means that the measured (back) face is recorded whereas it is the front face that is loaded. Measured values of velocity and inferred specific impulse are resultant from the stress wave propagating through the entire plate thickness. The methodology presented therefore, does not consider the effect this has on the spatial distribution of specific impulse.

Several steps have been undertaken within this study to ensure that validity of these assumptions are maintained or to minimise the effect that they may have on the results. Firstly the plate thickness was purposely designed to be as thin as possible across all tests, whilst still being able to withstand the load without significant petalling or fracture in the central region. By doing this, shear stiffness of the plate remains small such that the amount of energy dissipated as strain energy is minimised. It also maximises the proportion of energy imparted by loading that is converted to velocity uptake of the plate (i.e. a greater velocity for a given impulse). This mitigates the effects of assumption (i) that may cause non-physical skewing of the specific impulse data.

Reducing plate thickness was also designed to reduce the dissipation effects of assumption (iii). Figure 5 illustrates how a thinner plate means that the dissipated area on the

plate back-face is smaller. This means that smearing of information from the loaded front-face is reduced and the fidelity of spatial variations within the specific impulse distribution is retained.

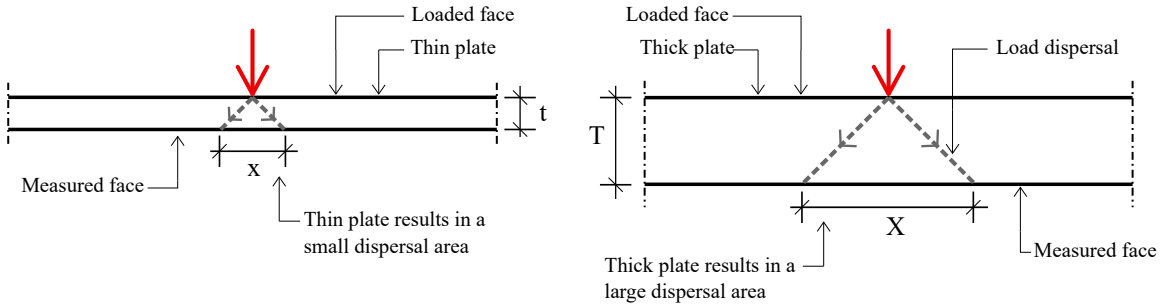

Figure 5: Illustration of the effects of plate thickness on through thickness load dispersal.

Assumption (ii) suggests that the peak velocity experienced by each subset is the initial velocity that is directly resultant from the specific impulse loading on that region. At later time periods within a test the velocity is likely affected by structural and boundary parameters. This means that selection of peak velocity requires careful consideration and this is discussed further within Section 3.3 of the discussion.

4 Results

The results from the experimental test series are presented in two separate categories: (i) qualitative assessment of plate deformation; (ii) transient displacement and velocity data directly outputted from the DIC algorithm.

4.1 Plate residual and transient deformation

A qualitative assessment and comparison of the failure and deformation modes of the plates across all test groups is made below.

Boundary tearing and failure mode

The test Groups can be divided into two categories defined by failure modes presented by Menkes & Opat (1973) and distinguished by the presence of boundary tearing:

- **Boundary torn tests** (Mode II failure): *Groups C, D and E* where the plate underwent tearing close to the clamping boundary causing it to fly out of the frame.
- **In-situ tests** (Mode I failure): *Groups A, B and F* where no tearing occurred and the plate remained within its clamping frame.

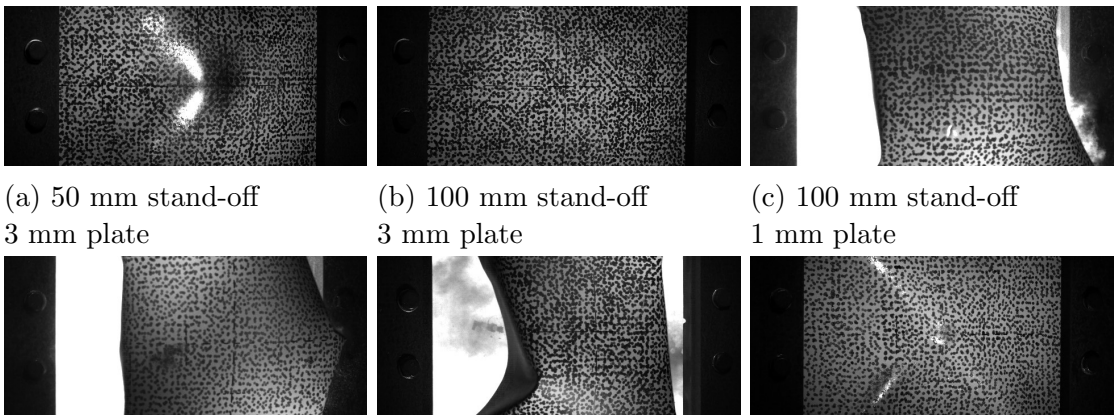

(a) 50 mm stand-off 3 mm plate

(b) 100 mm stand-off 3 mm plate

(c) 100 mm stand-off 1 mm plate

(d) 150 mm stand-off 1 mm plate

(e) 239 mm stand-off 1 mm plate

(f) 300 mm stand-off 1 mm plate

Figure 6: Late-time failure photos captured during tests.

Figure 6 depicts camera frames from individual tests of each group, after the shock load has passed (approximately 1 ms after detonation of the charge). This demonstrates the complete boundary tearing of Group C, D and E.

The time at which boundary tearing occurs (both partial and complete) was determined from the HSV footage and is shown in Figure 7. The pre-trigger region is also recorded in Figure 7 prior to the detonation time (0.4 ms). Time of tearing occurs later when stand-off distance increases (i.e. Group E undergoes tearing later than Group C with stand-off distances of 239 and 100 mm respectively). Group C appears to have a less variable spread of boundary tearing time than Groups D and E. This is particularly the case for the first initial tear and full tearing.

These results are extracted qualitatively from the HSV footage and could therefore be affected by an obscured or limited view of the boundary. The frame resolution does not cover the entire vertical boundary meaning the time at which the plate is fully torn could not be determined along its entire length. However, view of the boundary was deemed sufficient to demonstrate near-complete tearing of the boundary and was corroborated by rigid body motion of the plate in the camera frames thereafter.

Localised and global doming

Figure 8 presents transient cross-sections, demonstrating the plate deformation with time. These qualitatively describe the plate failure mechanism, from which features of the loading applied to the plate can be implied. Test Groups A-E all exhibited a global dome profile across the plate, with an increased degree of curvature present for tests of closer stand-off. These tests are assumed to experience greater loading magnitude.

Group A and C presented an additional central peak superposed on top of the global

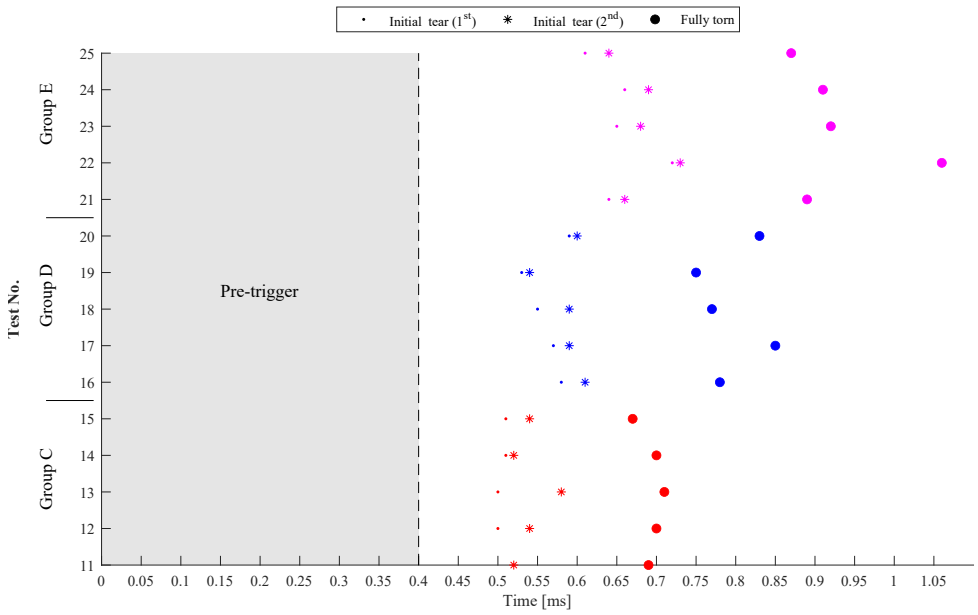

Figure 7: Figure presenting the time which partial (1^{st} and 2^{nd} boundary) and complete tearing of the plate occurs

dome which can be seen in the late time profiles in Figure 8a and c (presented as the darkest coloured cross section). The feature is likely caused by an increased localisation of the loading distribution when at shorter stand-off distances. Similar failure modes were seen within studies investigating localised blast loaded plate (Wierzbicki & Nurick 1996, Nurick & Radford 1997).

The early central deformation forms a shape profile that is similar to a gaussian curve. However, as the time progresses the concave region at quarter-span goes through significant deformation in the form of a "bulging" membrane action. This creates the global doming of the cross-section present in the final residual plate profile. Despite the increased deformation of the quarter span region, the central portion of the plate continues to move outwards and in-front of the global dome.

The Group F plates demonstrated X-shaped plastic yield lines converging to the plate centre from each corner. This is indicative of a spatially uniform load distribution being applied. Figure 9 shows the residual deformation on the loaded face for test groups A, B and F (in-situ tests) with Figure 9f clearly showing the yield line pattern. During the transient response shown in Figure 8f, the central region remained flat. Curvature and deformation was localised to an outer region which moves inwards towards the centre. This appears to represent a region of plasticity (plastic hinge) migrating from the boundary towards the centre forming the X-shaped yield lines seen in the residual shape profile.

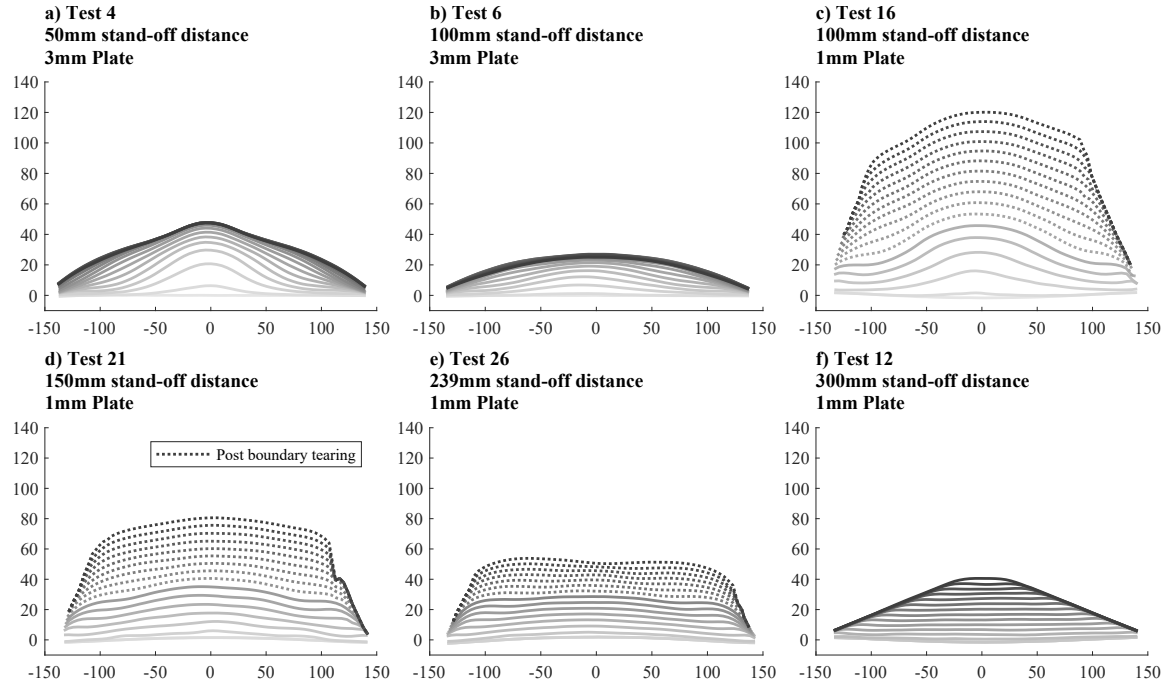

Figure 8: Cross section of the plate captured at 0.05 ms intervals (increasing line darkness illustrating increasing time) illustrating the change in displacement profile. Time after complete boundary tearing is demonstrated by dotted line cross-sections.

Localised melting of aluminium

Examination of the rear (loaded) face of plates from test Group A (photographed in Figure 9a) showed that the central region had lost its original smooth surface. It was instead irregular, with clear recesses and deformities. This is more prominent when compared with the loaded face of Group B and C seen in Figure 9b and 9c. This surface effect is potentially caused by localised melting of the aluminium due to the proximity of heat from the explosive detonation. Localised melting of the plate surface was also seen by Langdon et al. (2015) when blast testing aluminium alloy plates.

Paint spall

Several instances of paint spall that fit to a systematic trend were seen across the test groups. The measured face of Group A in Figure 6a shows that some paint spall occurred in a central region, due to the increased plastic strain in this area. Evidence of significant paint spall is present along the yield lines of Group F, as can be seen in Figure 6f.

It was noted within the HSV footage that seemingly random small areas of paint spall occurred within some tests early in the loading period. Whilst this could suggest weak adhesion of the paint in these regions it is also possible that this is representative of

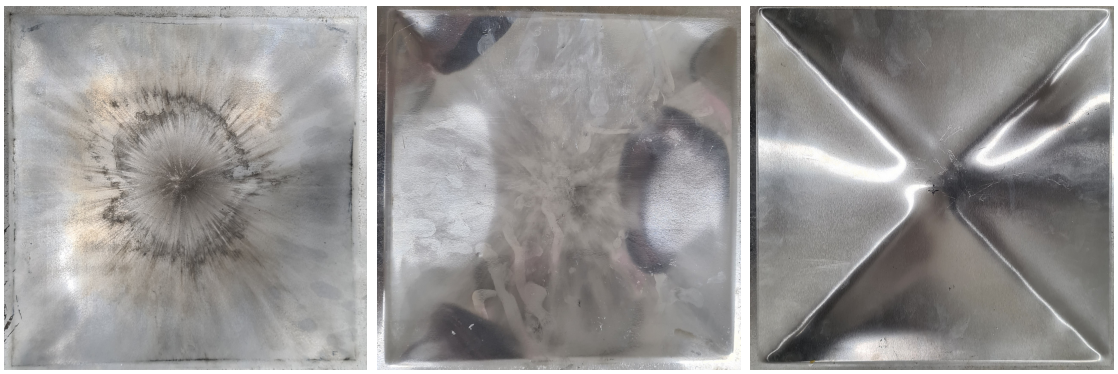

(a) Group A: 50 mm (b) Group B: 100 mm (c) Group F: 300 mm

Figure 9: Post-test photos showing the recorded the loaded face of the plate for the in-situ tests.

locally increased magnitude of loading. This appeared to be most prominent in Groups performed at intermediate stand-off distances (Groups C-E) and is potential evidence of complex interactions between the detonation product cloud and the shock-wave.

4.2 Transient midpoint behaviour

The averaged midpoint time histories for both displacement and velocity are presented in Figures 10 and 11. The values of displacement and velocity are averaged over a central region of 20 mm and are presented as a substitute for a discrete midpoint value. The data is expressed in this way as it is anticipated that protrusions and variability in spatial loading will occur within the near-field, as shown in the literature (Fuller et al. 2016, Rigby et al. 2019a). These have the potential to affect test repeatability of discrete points – averaging the midpoint values gives a more realistic comparison of test consistency.

Displacement data for the boundary torn (Mode II failure) tests (Groups C-E) is omitted as they are ejected from the clamp frame. This means they are subject to loss of optical focus and do not form a suitable means of comparison or appraisal of consistency. Group A displacement results are also omitted as the central paint spall results in premature data loss. However, it should be noted that paint spall occurs late enough that the Group A velocity recordings sufficiently capture the plates initial acceleration and response.

For comparison of all test groups Figure 12 shows both velocity and displacement histories for an individual test of each group. A summary of comparison points for the midpoint behaviour across the test groups are presented below.

Midpoint Displacement

Figure 10a presents the midpoint displacement response of all 5 tests from Group B and shows excellent agreement in the profile of displacement against time. This creates confidence in the consistency of the experimental methodology.

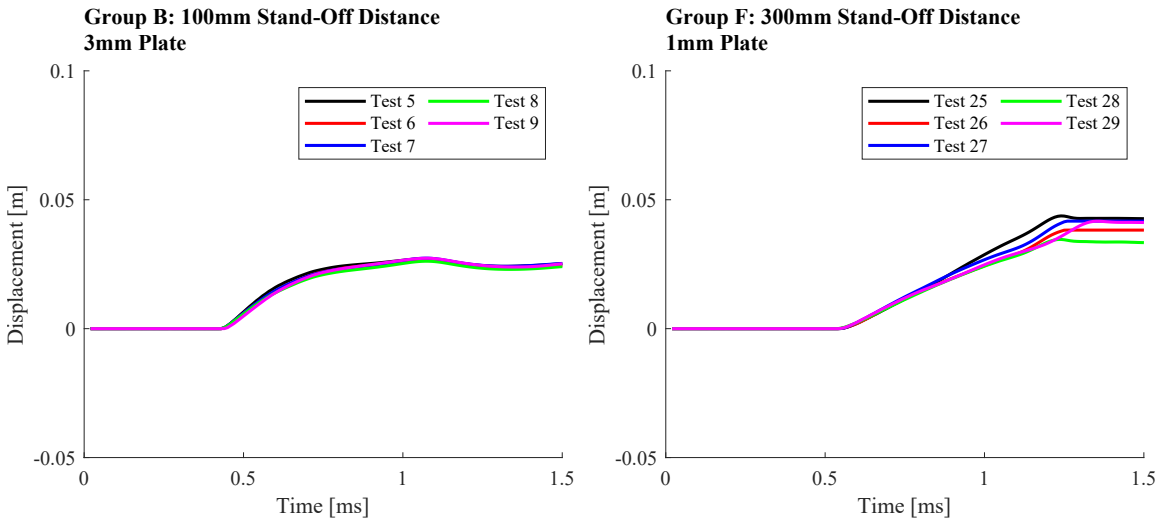

Figure 10: Displacement-time of tests at each stand-off distance which the plate remained in-situ within the clamping frame, averaged over the central 20 mm.

Figure 10b plots displacement-time histories for Group F and shows good agreement in the time of first acceleration and the initial gradient of the displacement time histories. However, at approximately 1 ms the curves begin to diverge and display a plateau behaviour. This region of the curves describes the point when the plate comes to rest.

It is postulated that the curves in Figure 10b diverge due to variation in the loading applied and the effects of the plate boundary. Variability in specific impulse across the plate may not be present at the midpoint, however its effect is seen after a plastic hinge forms at the boundary and translates in towards the centre of the plate. For this reason the displacement-time profiles begin to diverge at approximately 1 ms. This is after reasonable repeatability in the initial displacement responses. Rigby et al. (2020) suggested that larger scaled distances within the near-field are subject to more variable loading as a consequence of developing fluid-dynamic instabilities. This may explain the divergence of profiles in Group F (stand-off distance of 300 mm) when compared to Group B (100 mm stand-off distance). Plate thickness is also a potential factor as Group B utilised a thicker plate which has the potential to average the effects of variable loading.

Plates in Group F experienced significant paint spall, which was mainly present along X-shaped yield lines and in the central region. This paint spall occurs at a much later time, when a region of plasticity (plastic hinge) migrates in towards the centre.

Figure 12a presents the average midpoint behaviour for an individual test from each group. This shows how the displacement time behaviour is affected by stand-off distance increasing or changes in plate thickness. Analysing groups that use the 1 mm thick plate (Groups C-F), there is a trend of decreasing steepness of the initial gradient and a later time that the plate midpoint begins to deflect when stand-off distance increases. This trend is also present in the groups using the thicker 3 mm plate (Groups A and B).

Midpoint Velocity

The velocity time histories for the averaged mid-point (central 20 mm) are shown in Figure 11 for all 29 tests over the 6 test groupings.

All the curves exhibit an initial rapid rise to either a peak or close to peak value. Groups A-D (Figure 11a-d) all show a decay from this peak value down to a plateau. Groups A and B have a very short-duration of plateau (e.g. between 0.6 and 0.7 ms for Test 2 in Group A) followed by another decay. In Group B this deceleration results in a negative velocity at about 1.2 ms before a gentle rise to zero, whereas Group A decays directly to zero. Groups C and D have a continuing plateau which is ascribed to boundary tearing of the plate meaning they maintain velocity out of the clamp frame.

Peak behaviour in the velocity-time profile is described as a sharp gradient either side of the peak velocity, with this value also being significantly more than the resulting velocity plateau. This appears to be more significant at a closer stand-off distances. The relationship is particularly clear when comparing test using a 1 mm thick plate (Groups C-F) which show the value of peak velocity to increase with decreasing stand-off distance. This is attributed to an increased localised magnitude of the shock-wave as the target is moved closer to the charge.

The velocity-time histories in Figure 11 can be used as a means of comparing test-to-test variability. Group B (Figure 11b) has very repeatable results which echoes the findings in the displacement-time histories. Group E (Figure 11e) shows consistency in the entire velocity history, whilst group F (Figure 11f) is very similar across all the profiles up until approximately 0.8 ms, after which they begin to deviate. This indicates a variability in the structure's response to loading and the effect of boundary conditions rather than the loading itself.

Group A (Figure 11a) can not be compared over the entire measured time period due to central paint spall resulting in data loss. However, the peak values of velocity, the time of initial acceleration and the gradient of the first rise are consistent across the test groups. Groups C and D ((Figure 11c & 11d) have the most variation throughout the entire velocity-time history when compared with all the other test set-ups/groupings (excluding the Group A which lacks the full profile data to make a valid comparison). This is most prominent during the velocity peak, which suggests that the test-to-test variability is more evident at the intermediate stand-off distances at which Groups C and D were performed.

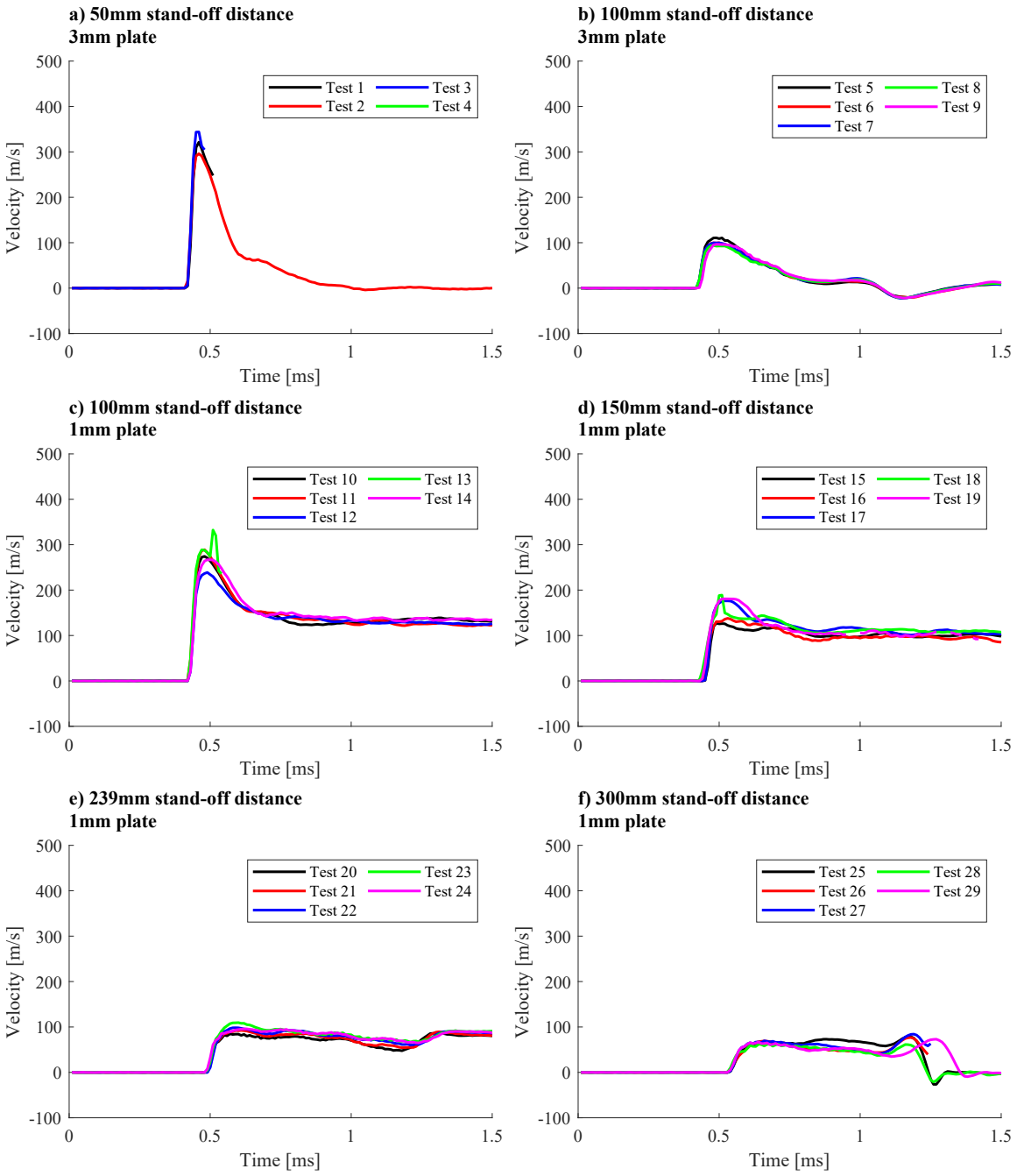

Figure 11: Velocity-time of tests at each stand-off distance which the plate remained in-situ within the clamping frame, averaged over the central 20 mm.

Figure 12b compares the midpoint velocity-time history from individual tests of each group. This shows the reduction in maximum velocity magnitude and increased distinction of the peak from the plateau behaviour as stand-off decreases. Stand-off is also shown to influence the time at which the midpoint first accelerates as this becomes later for greater stand-off distances.

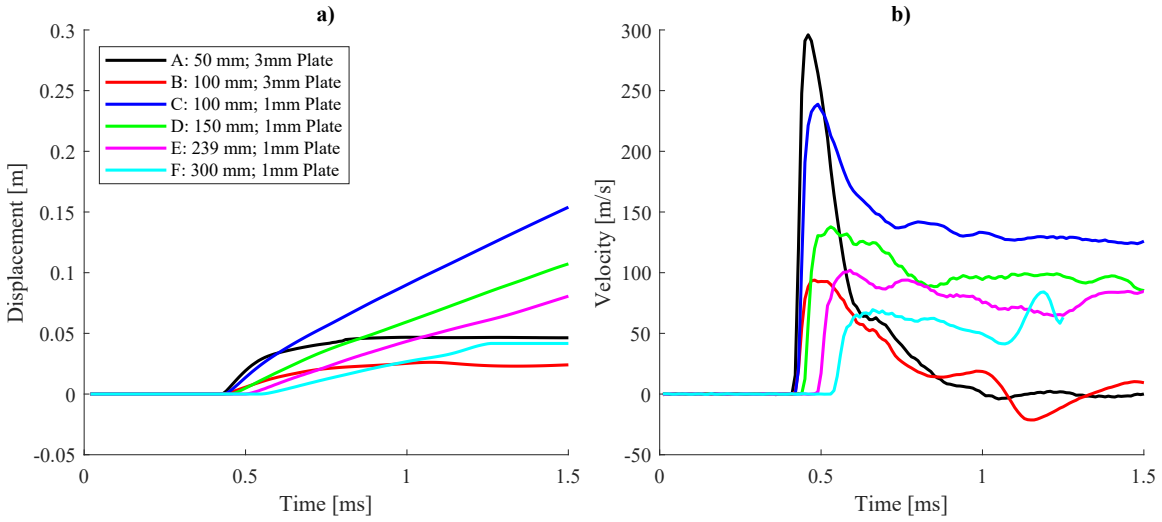

Figure 12: Displacement-time of an individual test at each stand-off distance which the plate remained in-situ within the clamping frame, averaged over the central 20 mm.

4.3 Velocity across the plate

Peak velocity forms the basis of the inferred specific impulse calculation that was presented in Section 3.3. As the aim of this study is to assess spatial distribution of loading it is important to investigate the velocity-time profiles across the plate surface. Figure 13 displays a midpoint, quarter-span (75 mm from centre) and edge (140 mm from centre) point for an individual test from each grouping. The positioning of these points across the plate surface is illustrated in Figure 14. Whilst each of the midpoint profiles matches with those seen in Figure 11 it can be seen that the quarter-span and edge points behave very differently compared to their associated centre point.

As previously discussed central velocity-time profiles for Groups A-D (Figures 13a-f) show a rapid rise to a peak velocity value followed by a decay. However, the quarter span point in test groupings A-D (Figure 13a-d) show an initial rapid rise, after which a reduction in the upwards gradient or plateau behaviour occurs. After this reduction in slope, the quarter-span point undergoes another secondary increase in velocity followed by a slight decay.

The secondary rise occurs at a far slower rate than the initial increase resulting in the peak velocity over the entire measured time-scale is reached at a far later time point

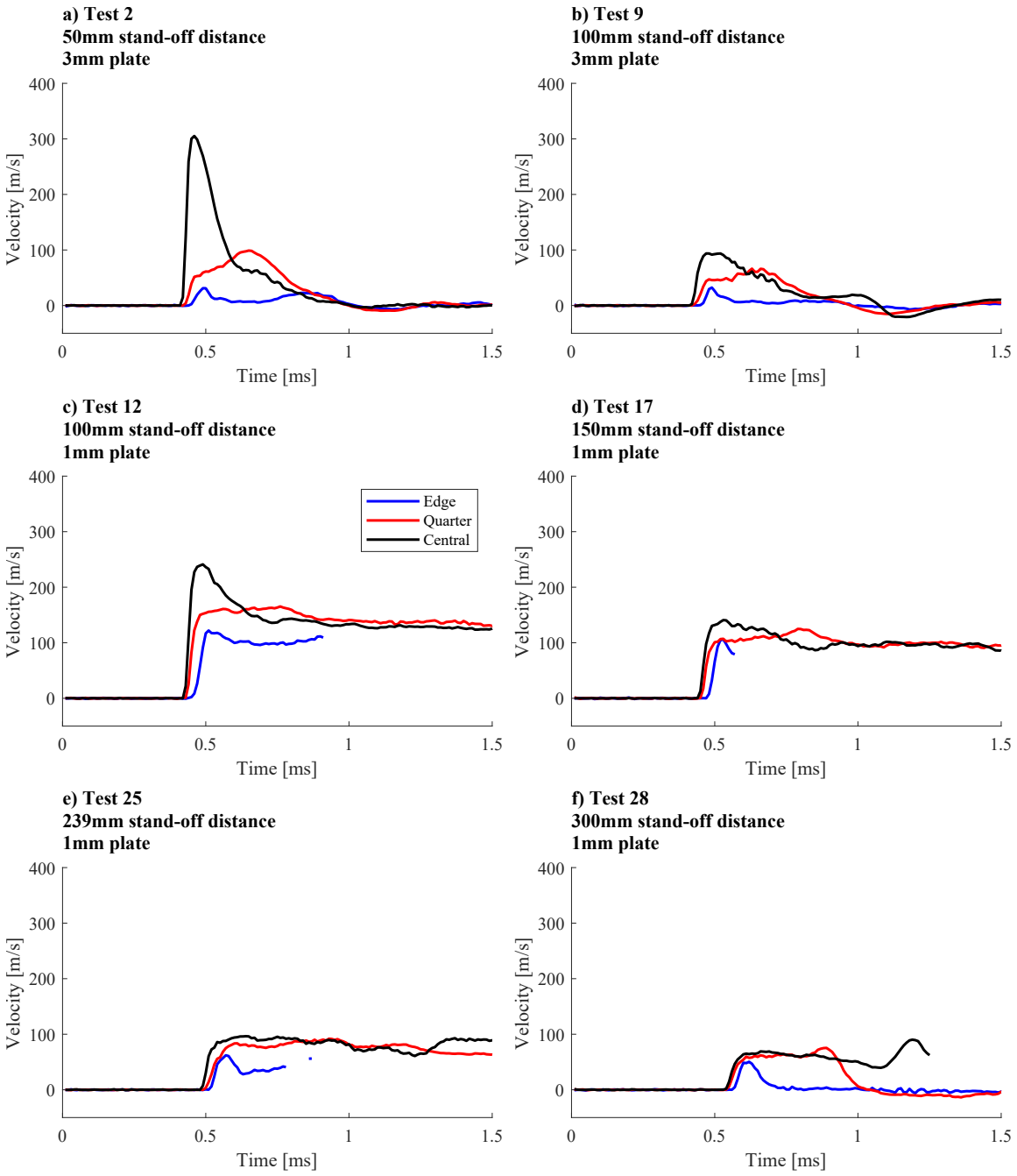

Figure 13: Velocity time histories taken from points positioned centrally, at the edge and at quarter span (0, 75 and 140 mm radial distance) for an individual test of each test grouping.

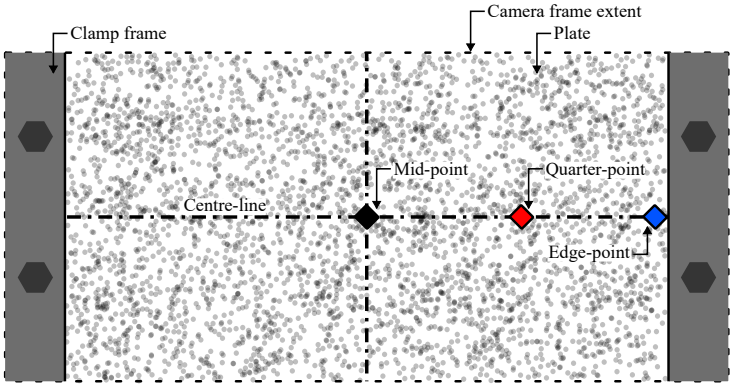

Figure 14: Illustration of the mid, quarter and edge point locations on the plate at 0, 75 and 140 mm from the plate centre respectively.

than is seen in the midpoint. If Figure 13a is considered, the midpoint peak velocity is reached at a time of approximately 0.5 ms whilst the peak velocity in the quarter span point occurs at approximately 0.7 ms. However, the time at which the initial first rise in velocity terminates (i.e. plateauing behaviour or reduction in gradient) in the quarter-span is similar to that of the peak in midpoint velocity.

The later time secondary peak occurring in the quarter-span velocity is of a slower rate and indicates a structural response effect. It is likely the load-structure interaction at the centre is being transferred across the plate and results in a secondary velocity increase later than when the shockwave and plate first interact. This effect is not present in test Groups E and F (Figure 13e-f) or to a degree that is not visible in the quarter-span profile. It is postulated that in the case of the smaller stand-off distances, central magnitude of impulse is of far greater magnitude relative to that at quarter-span. This means the shear transfer of the stress wave to the quarter-span has a greater effect on the velocity uptake at that point, albeit at a later time. The shear transfer effect to the quarter-span and how it varies with short and long stand-off distances (within the near-field range) is illustrated in Figure 15.

Notably, the edge point across all the test groupings does not show the same behaviour as that of quarter-span. In all the cases a clearly defined rise up to a peak velocity is seen. This occurs over a short time period, although at a slower rate and shallower gradient than that of the central and quarter-span points. This suggests a decrease in loading magnitude at the points adjacent to the plate's edge. After the peak is reached all the edge point curves decay down to a plateau unless data is lost prior to this (Figures 13d and e). It should be noted that the edge points were most susceptible to paint spall and data loss earlier within the test. This was due to the boundary tearing and inward folding that occurred at this point. Significantly though all edge points show a very distinct peak velocity followed by a prominent deceleration that can be easily identified.

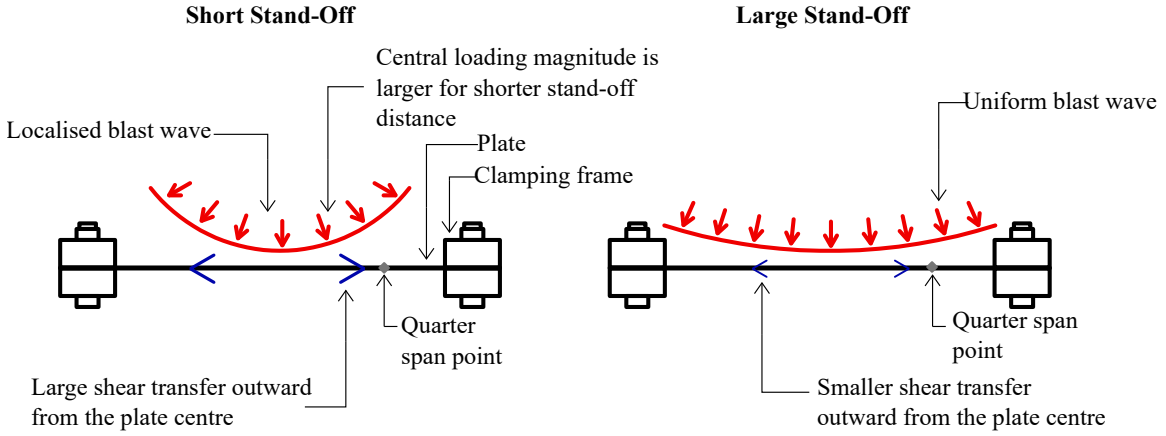

Figure 15: Illustration of the shear transfer out from the centre of the plate to the quarter span and how this varies and short for long stand-off distances.

4.4 Plastic hinge

If the velocity time profiles from test Group F (the largest stand-off test) for both the averaged midpoint and across the entire plate (Figure 11f and 13f) are analysed, a late-time acceleration to a peak velocity is observed. This is followed by a rapid deceleration to a negative velocity before correcting back to zero. In Figure 11f the peak of this feature occurs at a time of 1.15-1.30 ms and appears to be very consistent across the majority of tests, however there is approximately 0.9 ms time lag on Test 30. If this feature is examined across the plate in Figure 13f it occurs in the quarter-span point far earlier than it does at centre (0.88 ms relative to 1.19 ms) however, it is not seen at all in the edge point curve. This could be due to data loss or paint spall prior to the effect being captured.

Plastic hinge effects are not evident at all either centrally or across the plate in test groupings C-E (notably these are the boundary torn tests, where the plate is not brought to rest within the clamping frame). Test Group B has a similar feature without as large a peak as in Groups E and F. However, there is a region where both the central and quarter-span point decelerate and reach a negative velocity before accelerating back to zero. Test Group A loses data centrally too soon after the first peak across most of the tests for this feature to be seen. It also is not observed in Test 2 which does retain data throughout the entirety of the test as seen in Figure 11a.

It is believed that this secondary peak in velocity, followed by the negative deceleration is caused by the inwards migration of a plastic hinge from the edge of the plate. This effect can be seen in Figure 16 (showing Test 29 in Group F) where a banding of increased velocity forms at the edge of the plate, which proceeds to move in towards the centre. After, this band has passed there is a small region of negative velocity before the plate is brought to rest. This behaviour was also observed and commented upon by Curry et al.

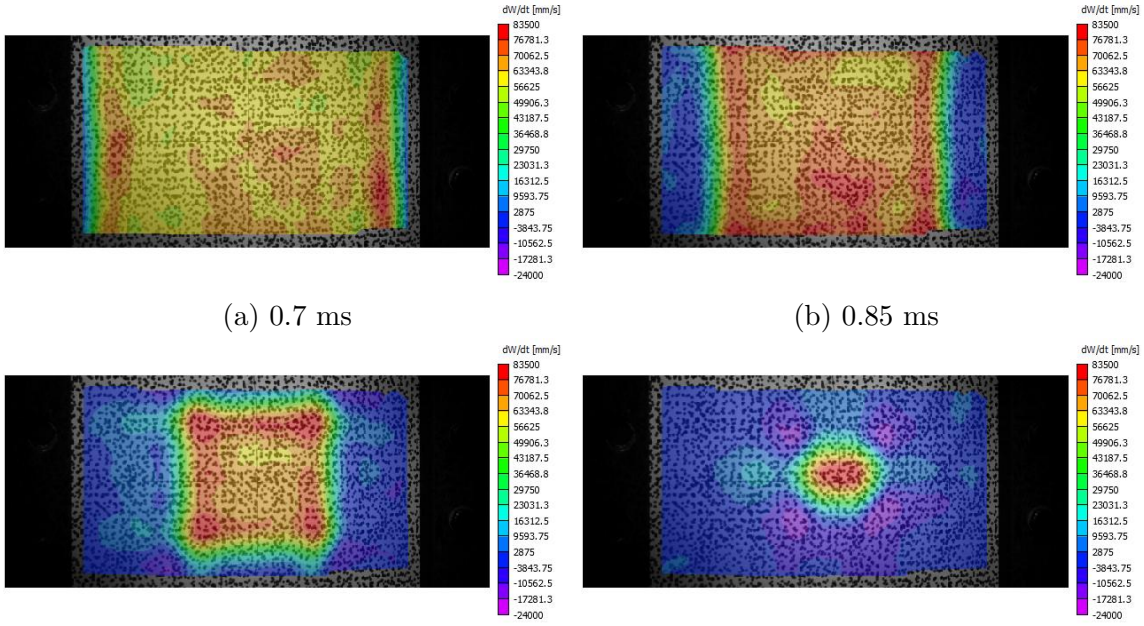

(a) 0.7 ms (b) 0.85 ms

(c) 1 ms (d) 1.15 ms

Figure 16: Test 26 velocity contours plotted over plate speckle image frames illustrating the migration of the plastic hinge converging to the centre.

(2025).

5 Discussion

5.1 Uncoupling loading effect and structural response

The method for calculating specific impulse was presented in Section 3.3, based upon studies by Rigby et al. (2019a) and Curry et al. (2025). Rigby et al. (2019a) performed DIC with HSV recordings limited to 30 kfps meaning the structural response features in the velocity history had the potential to affect the peak velocity value used to calculate specific impulse. This limitation was highlighted by Curry et al. (2025) who utilised 100 kfps HSV recordings. The greater frame rate and therefore number of transient data points, provides substantially more information about the development of velocity with time. The following discussion concerns itself with uncoupling the loading effect and structural response to maintain confidence in the specific impulse values calculated. Whilst Curry et al. (2025) utilised shear wave speed theory for this reason, this was only demonstrated for extremely close proximity charges ($<0.162\text{m/kg}^{1/3}$). This study discusses the process for a far large range of near-field scaled distances.

Whilst the resultant response of the plate is affected by fluid-structure interaction,

testing of two different plate thicknesses at the same stand-off distance (Groups B and C) provides an insight into how this effect manifests in the inferred loading. When considering the velocity-time history, it can be described by two phases based upon the influencing factors on the plate's behaviour:

Loading effect

This time period encompasses the early stages of the structure's response (near-instantaneous application of a peak velocity) such that shear transfer of the load has not yet taken place and therefore the velocity is purely a product of the loading and is minimally influenced by the plate characteristics and its boundary. It should still be noted that through-thickness dissipation of the load is a factor as discussed in assumption (ii) of Section 3.3. However, it is in this period that the peak velocity should be sampled, to ensure that the calculated specific impulse is not artificially skewed by accelerations in the plate that are a result of the structure's response and not the loading. In the velocity-time histories presented as examples in Figure 13, this period encompasses the peak of the initial rapid rise in the velocity.

Structural response

In this phase the velocity response is considered a product of both the applied loading and structural features such as boundary effects. Once loading has been applied to the structure, it responds through a shear transfer of stress out towards the boundary where regions of plasticity or yielding begin to occur. This can result in boundary tearing or the plasticity migrates inwards in a band of increased velocity (plastic hinge) as seen in Figure 16. This results in a secondary peak of velocity in many of the velocity-time histories (particularly visible in Figure 13), after the initial rapid rise has occurred. If sampled as the peak velocity these features could artificially skew the calculated specific impulse as it is affected by the boundary and plate characteristics instead of the loading. This region is displayed as the period after the initial first rise and includes any secondary peaks of a slower acceleration (gradient) than that seen initially.

5.2 Sampling peak velocity

Discerning the *loading effect* and *structural response* regions from one another in a qualitative manner is simple in the case of a single or small number of data points. However, as every test in this study encompasses more than 2100 data points a systematic way of uncoupling the loading effect and distinguishing these regions in a way that is physically valid must be determined. It is important to separate these regions as the peak velocity sampled from the entire velocity-time history (to be used to calculate specific impulse) can sometimes be taken from the *structural response* region and is therefore, not a physical

representation of loading. Instead the peak velocity must be sampled from the *loading effect* region rather than that of the whole range in order to prevent structural features (e.g. secondary peaking caused by loading of central regions, plastic hinge inwards migration) from influencing the inferred specific impulse values.

In order to, systematically separate the loading effect region, the period of loading needs to be defined – which requires two parameters to be determined: (i) time of first acceleration and (ii) time of loading end, as described below.

Time of first acceleration

The time of first acceleration is the first point in the DIC algorithm where it can be determined the plate is accelerating and therefore loading has been applied. This is similar to the time of arrival (t_a) used when considering pressure-time histories measured by a standard piezo-resistive or piezo-electric pressure gauge (Farrimond et al. 2022). The time of first acceleration $t_{acc.}$ differs from the time of arrival as it includes the pre-trigger region ($t_{trig.} = 0.4$ ms) and the time taken for the stress wave to travel through the plate's thickness and insight an acceleration in the plate's back face (referred to as time of plate reaction, t_{plate}).

$$t_{acc.} = t_{trig.} + t_a + t_{plate} \tag{2}$$

Due to the spatial variability of loading (including central localisation) this value can potentially vary significantly across the plate with it being anticipated that $t_{acc.}$ is shorter for central regions of the plate than it is for the edge (this is depicted by the beginning of the first rise in the velocity-time profiles of Figure 13). The time of first acceleration therefore provides important information on the spatial characteristics of loading and also defines the beginning of the loading effect region of the velocity-time profile.

The maximum pre-trigger noise was calculated to be 5×10^8 mm/s^2 and was used as a threshold value to determine the time of first acceleration. This meant the point in the velocity time profile at which the initial rapid rise was taken could be found and therefore provided the corresponding time of first acceleration for each data point. For determining the period of time the plate is undergoing loading, the time of first acceleration was computed for the central 20 mm region as this should be loaded first (considering the theory of a centrally localised blast load amounting from a spherically expanding blast wave). The averaged region was selected to limit the potential for early-time protrusions and instabilities in the fireball to skew the extracted value as these would result in a time that is earlier than the main shock-wave. These values were then formed into data distributions based upon the test groupings (i.e. each stand-off distance) and the average value was taken as the time of first acceleration.

Time of loading end

The time of loading end can be considered the point at which the loading effect region terminates and the structural response period begins (i.e. after the peak of the first initial rise). This is more complicated to define than the time of first acceleration as it has to consider two characteristics: (i) the secondary peaking effect seen in the quarter-span points caused by outward shear transfer of loading from central regions (particularly for tests of smaller stand-off distances as shown in Figure 13) and (ii) inwards migration of the plastic hinge as seen in Group F in Figures 13f and 11f.

By once again considering the blast wave and fireball as an outwardly propagating sphere the edge of the plate should undergo loading last. This suggests that once edge points of the plate have decelerated then the plate movement is only subject to the structural response and loading has ceased. Furthermore, the edge point velocity-time histories displayed in Figure 13 show a far clearer peak followed by a deceleration, than that of the quarter span. It can therefore, be considered that after the first deceleration of the edge point all loading effects have taken place and after this point velocity increases are a feature of the structure and clamp.

The first deceleration after $t_{acc.}$ was recorded for each of the points 140±1 mm from the plate centre (this being the edge of the recorded region). Due to the large number of data points outputted by the DIC algorithm, the data distribution is sufficiently populated to demonstrate a normal distribution across each of the test groupings and therefore, the mean value is used henceforth with some confidence. This mean value of edge deceleration time is denoted as t_{ED}.

Table 3: Values of time determined as the upper and lower bounds of the frame range (time period) which peak velocity is sampled from.

Group	**Stand-off**	**Plate thickness**	**Time of first acc.**	**Sample range end**
	mm	mm	ms	ms
A	50	3	0.40	0.50
B	100	3	0.41	0.51
C	100	1	0.41	0.53
D	150	1	0.43	0.55
E	239	1	0.48	0.60
F	300	1	0.53	0.64

This method demonstrates the benefit of the large amount of data points generated from DIC instrumentation which would not be possible in other experimental techniques. Unlike the shear wave migration method presented by Curry et al. (2025), it is also based

upon an experimental measure, not purely on a theoretical calculation. This is significant as the blast loading in the intermediate near-field is complex in character and therefore is unlikely to be easily defined by analytical approaches. When utilising the shear wave method (Curry et al. 2025) the velocity sampling range would frequently terminate prior to the end of the first velocity peak (i.e. before the *loading effect* region had finished) for tests at larger scaled distances (150-300 mm). This suggests that the method for sampling velocity used by Curry et al. (2025) is only suitable for extremely close proximity stand-off, as the maximum scaled distance they tested was 0.163 m/kg$^{1/3}$.

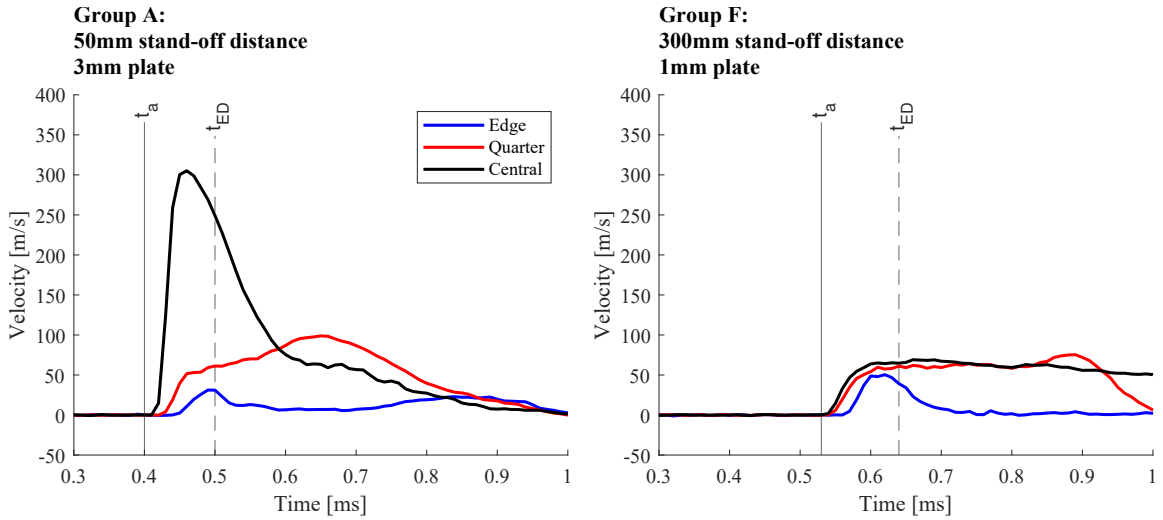

Figure 17: Demonstration of the calculated sampling range for velocity sampling ranges. This is a presentation of Figure 13 where the x-axis range has been reduced and the velocity sampling ranges are presented.

5.3 Loading curves

Specific impulse can be determined for each of the DIC spatial data points (c.2100) extracted per test. Figure 18 demonstrates specific impulse values plotted against radial distance from plate centre for an individual test from Group A and F (smallest and largest stand-off distance).

Figure 18 only represents a portion of the accrued data, yet it showcases the high density of data points that is achieved across a single test. Interestingly there are regions of substantially denser data points (suggesting more consistent loading) and areas that are more sparse (suggesting localised increases or decreases away from the average). These features and the spread of magnitude for a given test shows that the loading experienced across the plate is not smooth or idealised. Instead there are regions where the loading results are subject to more variation. This can be seen clearly throughout Group

A (Figure 18a) where the upper-bound of the data undulates across the profile. This suggests that to represent this data accurately, specific impulse values must be treated as a distribution of data where the mean and degree of variance (spread) is shown.

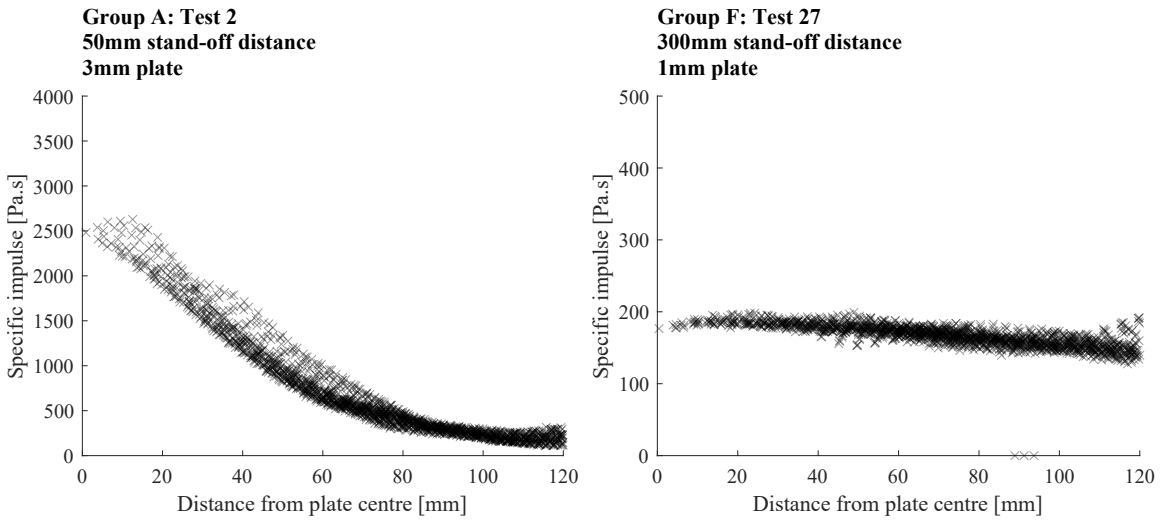

Figure 18: Specific impulse against radial distance from centre distributions inferred from the velocity profiles for an individual test at each stand-off distance.

For the purpose of test-to-test comparison an effort was made to condense the data from each individual test into a simpler form that still represented the load distribution as whole, including its variation. To do this the data was sub-divided into bins of 5 mm increments out from the plate centre. Within each of these bins there now exists a data distribution of specific impulse values, from which a mean and standard deviation can be calculated. The size of the bins was selected to ensure sufficient data to describe the distribution whilst retaining spatial resolution and fidelity. From these mean values a specific impulse profile against radial distance out from centre can be plotted, as shown in Figure 19. Additionally the first standard deviation either side of the mean profile is plotted as a shaded region to give an appreciation of spread within the whole data distribution. Figure 19 encapsulates the entire test series sub-divided into their test groupings with each curve representing an individual test.

The loading profiles in Figure 19 corroborate the trend of greater central localisation and specific impulse magnitude occurring at smaller stand-off distances. The effects of localised loading on plates have been demonstrated (Wierzbicki & Nurick 1996, Chung Kim Yuen et al. 2017) and various experimental studies have assessed loading at close proximity (Rigby et al. 2019a, Qi et al. 2024, Curry et al. 2025). However, the results in Figure 19 fully describe the profile of loading and how this changes throughout the near-field range of scaled distances in a way that is not experimentally determined within the existing literature.

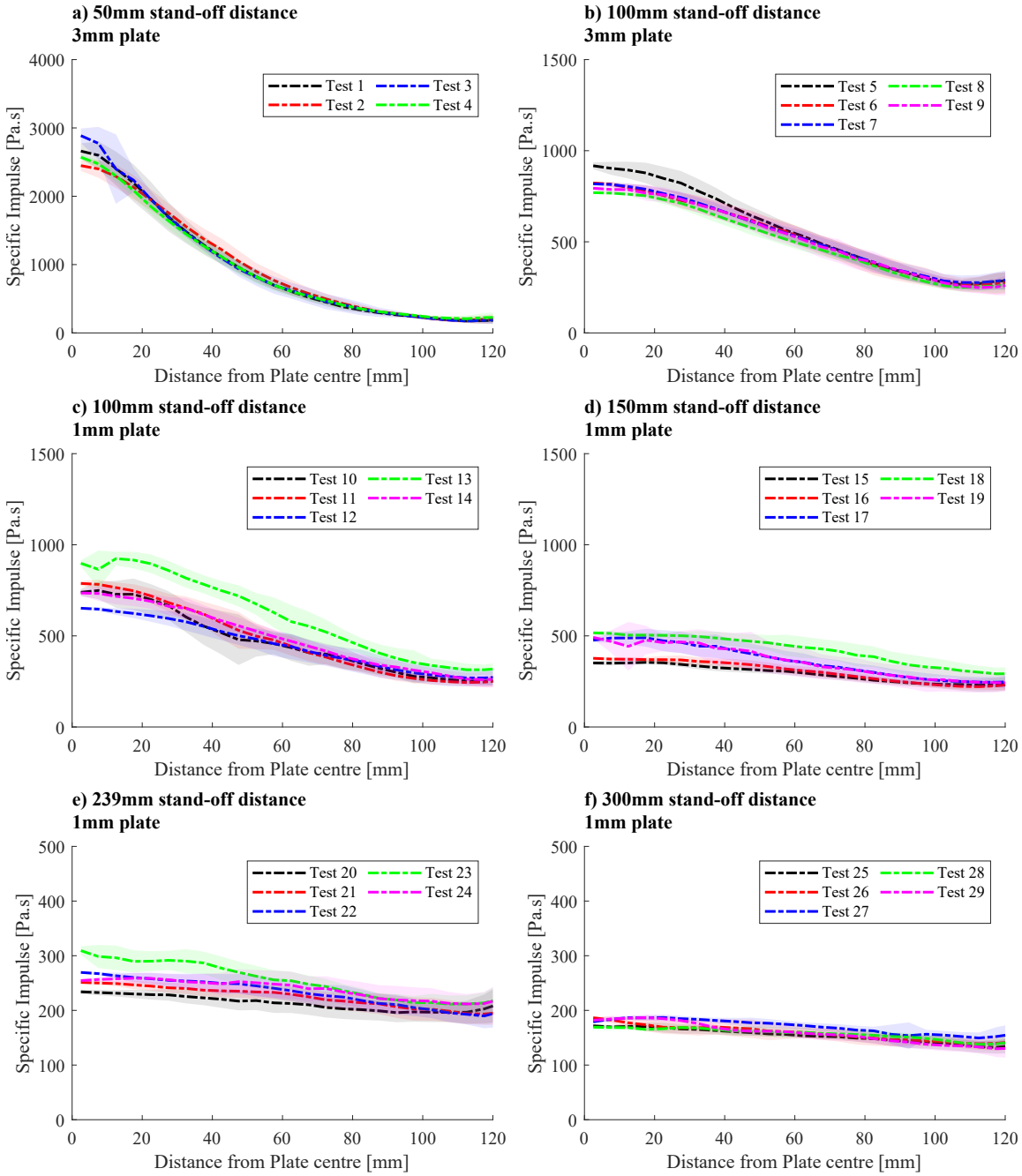

Figure 19: Specific impulse distributions of all test formed by consolidating the data seen in Figure 18 into 5 mm bins where the mean for each band is plotted and the first standard deviation is shown within the shaded region.

Figures 19a-c represent the closer stand-off distances and exhibit a loading profile that is similar to a Gaussian curve in shape, although Figure 19a is noticeably sharper and more narrow. Figures 19d-f show the larger stand-off distances and exhibit a far more uniform load profile. The results suggest that after a scaled distance of 1 m/kg$^{1/3}$ the loading profile can be considered near-uniform at this scale. Whilst the relationship between central localisation and stand-off distance is expected these results present it at a resolution and detail that is not possible without the use of full-field optical methods such as DIC.

5.4 Global impulse

The specific impulse data was used to calculate global impulse across an area of 100×65 mm on the plate. This area was selected due to the extent of the vertical camera frame and limit any boundary effects on the calculated impulse values, resulting in the most consistent comparison. The results are presented in Figure 20a against the corresponding scaled distance of each test. A trend of exponentially decaying impulse with scaled distance is seen in these results. The plate thickness does not appear to influence the recorded impulse; examining Figure 20a at a scaled distance of 0.34 m/kg$^{1/3}$ shows the 3 mm plate recordings (Group B) fits within the range determined from 1 mm thick plates (Group C).

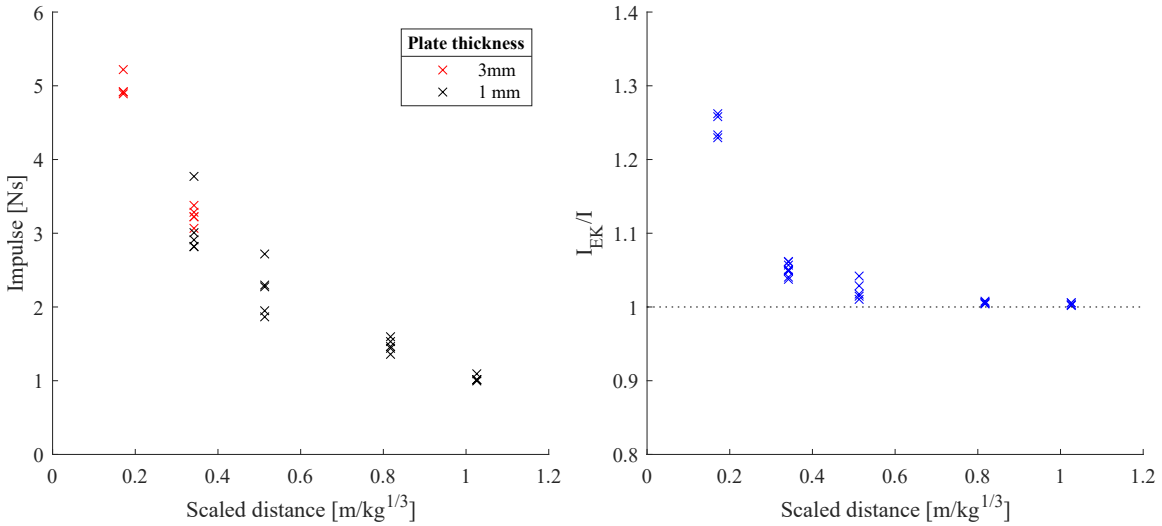

Figure 20: (a) Impulse across a 100×65 mm region of the plate for each test plotted against its corresponding scaled distance. (b) Ratio of energy equivalent global impulse calculated using the methodology presented by Rigby et al. (2019b) plotted against scaled distance

Rigby et al. (2019b) presented an energy equivalent impulse, I_{EK} (determined us-

ing equation 3) that is representative of an "energy-averaged impulse as opposed to a spatially-averaged impulse". This parameter was used to assess spatial non-uniformity of a distributed loading. The energy equivalent impulse was used by Rigby et al. (2019b) to rationalise a localised or non-uniform loading into an evenly distributed one. The ratio of energy equivalent impulse to the experimentally measured impulse is a measure of spatial uniformity of the loading (a ratio of 1 means the loading is perfectly uniform and larger ratio corresponds to greater non-uniformity of the load distribution).

It has been shown previously that applying an energy equivalent uniform impulse to a deformable plate results in remarkably similar peak and residual deflections compared to plates under the full loading distribution (Rigby et al. 2019b, Alotaibi et al. 2023). This is highly significant for two reasons: first, it is a clear demonstration that both the loading and magnitude of an impulsive load must be known in order to accurately model plate deformation; second, there is now an accurate method based on simple physical laws which enables a complex distributed load to be transformed into an equivalent uniform load. Being able to transform the loading into a single-number equivalent allows for distributed loads to be input into single degree of freedom analyses, or other simple plate response predictors such as that of Nurick & Martin (1989).

$$I_{EK} = \sqrt{A \int_A \frac{(idA)^2}{dA}} \tag{3}$$

Figure 20b shows the ratio of energy equivalent impulse against the global impulse values of Figure 20a. The data charts the relationship of non-uniformity with scaled distance as it tends towards 1. The closest scaled distance results in a high ratio of approximately 1.25, demonstrating a highly non-uniform distribution which is evident from the loading curves in Figure 19a. After a scaled distance of approximately 0.8 m/kg$^{1/3}$ the loading can be considered almost completely uniform.

5.5 Variability

The loading distributions in Figure 19 were used to appraise variability and how this is affected by scaled distance. Comparing nominally identical tests from each grouping shows them to be consistent in shape profile and magnitude. This creates confidence in the repeatability of the experimental method, however there is clear variability present throughout the scaled distances tested. Test 14 sits noticeably apart from the other tests within Group C (Figure 19c) which suggests potential turbulent effects from the fireball have caused an increased loading. This demonstrates that variabilities in close proximity blast loading should be considered; a deterministic assessment is insufficient to describe the potential impulse that a structure may experience. Significantly, the tests performed at the largest stand-off distance (Figure 19f) are remarkably similar and appear to be more consistent than those of the other test groupings suggesting that loading at this distance

is subject to less variability. At this point it is likely that fireball interaction with the shock loading has either ceased (blast wave detachment) or become far less significant.

Table 4: Statistical parameters demonstrating the variability of specific impulse results within the data bin for all tests across a group positioned at 0 and 60 mm from plate centre. Z denotes the scaled distance, μ the mean, σ the standard deviation and Q_{range} is the quantile range

Group	**Stand-off**	**Z**	$\boldsymbol{\mu}$	$\boldsymbol{\sigma/\mu}$	$\boldsymbol{Q_{range}/\mu}$	
					25-75%	**5-95**%
	mm	m/kg$^{1/3}$	Pa.s	Pa.s		
Centre						
A	50	0.171	2641	0.07	0.09	0.23
B	100	0.342	824	0.06	0.05	0.21
C	100	0.342	759	0.11	0.13	0.35
D	150	0.513	445	0.15	0.29	0.41
E	239	0.817	262	0.10	0.08	0.32
F	300	1.026	178	0.04	0.05	0.13
60 mm from plate centre						
A	50	0.171	660	0.15	0.19	0.53
B	100	0.342	525	0.09	0.13	0.32
C	100	0.342	486	0.18	0.23	0.57
D	150	0.513	355	0.20	0.29	0.57
E	239	0.817	236	0.10	0.13	0.35
F	300	1.026	161	0.06	0.08	0.20

Table 4 presents statistical measures of variability (namely standard deviation and quantile ranges normalised against the mean) calculated from bins placed centrally on the plate and at 60 mm from centre. The data distributions were extracted from all tests for a given group, to demonstrate how variation is affected by scaled distance. The values in Table 4 are summarised in Figure 21 against scaled distance.

By examining the normalised standard deviation and quantile ranges in Table 4 and Figure 21 it can be seen that groups C-E have the largest variability. This coincides with intermediate scaled distances within the near-field (0.34-0.82 m/kg$^{1/3}$). It also agrees with the suggestion by Rigby et al. (2020) that instabilities within the fireball undergo development stages and become more significant within the intermediate near-field. These in turn influence the loading variability.

Group F shows a clear decrease in variation which is potentially caused by detachment of the shockwave from the fireball or reduced effects of instabilities within the fireball on

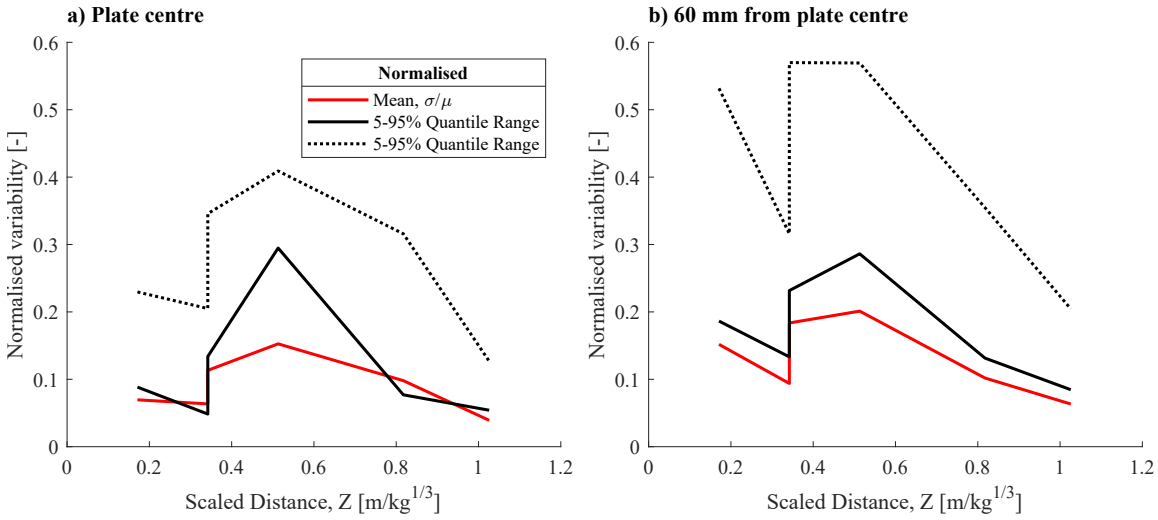

Figure 21: Normalised statistical variability parameters (standard deviation as well as quantile ranges of 25-75% and 5-95%) extracted from each test group plotted against the associated scaled distance. Values correspond to those shown in Table 4.

the loading. The spatial variations in the loading curves are notable as local magnitude increases coinciding with weak points in a structure could have catastrophic results on their protective functionality.

5.6 Plate thickness effects

The effects of plate properties can be considered by comparing Group B and C (Figures 19b and c) which are tests of the same stand-off distance but different plate thicknesses. A comparison between the entire datasets of Group B and C is made in Figure 22 with the mean presented alongside the 95% and 5% quantiles. Inspecting Figure 22 shows that Group B has a greater magnitude of specific impulse in the central regions and across most of the distribution. One explanation for this is that reduced deflection in the thicker plate causes the impinging pressure and impulse of the shock-wave on the plate surface to be closer to a fully reflected value. The greater deflection of the thinner plates (Group C) causes relief of the pressure and a reduced specific impulse magnitude is inferred. This would be representative of fluid structure interaction where the plate deforms within the loading duration, affecting the flow of pressure and impulse. This would also explain why the discrepancy between the mean magnitudes is greatest centrally and reduces outwards, as the the difference in deflection between the thick and thin plates follows a similar trend (greatest difference at the centre and least at the plate edge).

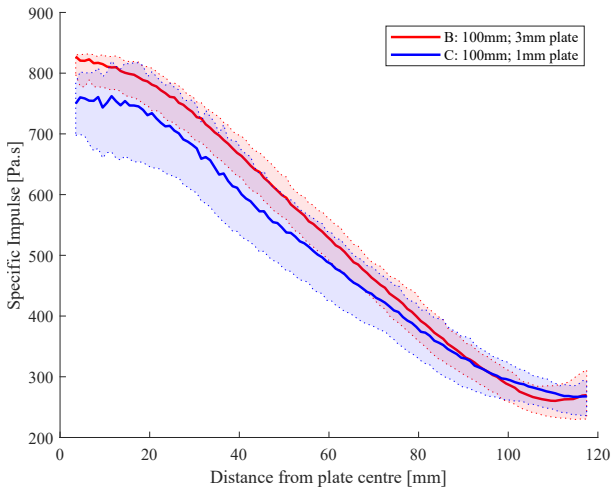

Figure 22: Specific impulse distributions presented as the mean alongside the 95% and 5% quantiles calculated from 5 mm bins of radial distance.

It should be noted that the thinner plates in Group C have a wider spread of magnitude throughout the distribution and that the majority of the Group B dataset falls within its extents. This suggests that the the impinging shock is subject to variation in magnitude and the thinner plate is more sensitive to this (as it more closely obeys assumption (i) and (ii) in Section 3.3).

The results shown in Figure 22 demonstrate that plate thickness has an effect on the magnitude of loading inferred from the DIC methodology. However, it does demonstrate that the shape profile of the distributions is fairly consistent and that investigating the influence of plate thickness in this manner provides insight into fluid-structure interaction.

To fully assess the effects of this, further tests on a greater number of plate thicknesses would be required.

6 Conclusion

This study focussed on the characterisation of specific impulse distributions from near-field blast loading. Digital Image Correlation was used to record plate deformation at high spatial (2,100 points) and temporal (100,000 fps) resolution, at 5 different scaled distances across the near-field range (0.17–1.03 m/kg$^{1/3}$). 29 tests were performed in total, with measured initial velocities used to infer imparted specific impulse distributions through conservation of momentum. This resulted in highly detailed loading maps across a comprehensive range of scaled distances, allowing several key behaviours to be observed.

First, loading profiles in the extreme near-field were shown to be highly localised and approximately gaussian in shape, with the loading becoming lower in magnitude and flatter in distribution as scaled distance increased. This was corroborated by post-test plate surveys which revealed the residual plate deformations in the extreme near-field to resemble a global dome with central dishing (consistent with a centrally localised load), and with residual plate deformations in the late near-field resembling an X-shaped yield line pattern, characteristic of spatially uniform pulse loads.

Secondly, whilst the shapes of loading distribution were consistent for a given scaled distance, there were noticeable test-to-test variations in magnitude, made more significant by the existence of highly localised enhancements in loading. These features are postulated to be caused by complex interactions between the expanding detonation product cloud and the attached shock wave, resulting in the formation of instabilities and protrusions which have been observed in previous near-field testing but not characterised with the detail and rigour achieved herein. These localised features were seen to vary with scaled distance, being most significant at intermediate near-field scaled distances and being generally negligible at both the extreme and late near-field scaled distances.

Practical considerations were shown to increase the reliability and validity of the test procedure. Namely, reducing plate thickness was seen to increase the measured spread of loading, suggesting that a thinner plate is more sensitive to the presence of the afore-mentioned localised variabilities (i.e. a thicker plate acts to somewhat "dampen" these features and therefore the velocity uptake is much more consistent). Methodical sampling of peak velocity was shown to be necessary in order to prevent structural effects from spuriously augmenting the inferred specific. This was done by assessing the time at which the plate edge was seen to decelerate for the first time, and assuming this to be the point at which all loading has been imparted to the plate. This post-processing step was shown to substantially improve the accuracy and validity of the measured impulse distributions.

The technique and experimental observations presented in this article allow for a more comprehensive and fundamental study into the nature of near-field blast loading, with a

view to ultimately developing more accurate and robust predictive techniques to both model and replicate these complex loading behaviours.

Acknowledgements: The authors acknowledge the technical aid of A. Hibbert, S. Woolford, J. Hibbert, T. Lodge and D. Farrimond as well as the funding of this research project by the US ERDC under contract BAA W912HZ21C0036.

Data access statement

Data presented within this article can be requested from the corresponding author at l.p.tetlow@sheffield.ac.uk.

Compliance with ethical standards

Conflict of interest: The authors declare that they have no conflict of interest.

References

Alotaibi, S. A., Rigby, S. E., Guadagnini, M. & Tyas, A. (2023), 'Rigid-plastic membrane response of thin plates under impulsive blast loads using the extended hamilton principle', *International Journal of Impact Engineering* **178**, 104624.
URL: *https://www.sciencedirect.com/science/article/pii/S0734743X23001355*

ASM Handbook Committee (1990), *Properties and Selection: Nonferrous Alloys and Special-Purpose Materials*, ASM International.
URL: *https://doi.org/10.31399/asm.hb.v02.9781627081627*

Aune, V., Fagerholt, E., Hauge, K., Langseth, M. & Børvik, T. (2016), 'Experimental study on the response of thin aluminium and steel plates subjected to airblast loading', *International Journal of Impact Engineering* **90**, 106–121.
URL: *https://www.sciencedirect.com/science/article/pii/S0734743X15300099*

Balakrishnan, K., Genin, F., Nance, D. V. & Menon, S. (2010), 'Numerical study of blast characteristics from detonation of homogeneous explosives', *Shock Waves* **20**(2), 147–162.

Barr, A. D., Rigby, S. E., Clarke, S. D., Farrimond, D. & Tyas, A. (2023), 'Temporally and spatially resolved reflected overpressure measurements in the extreme near field', *Sensors* **23**(2).
URL: *https://www.mdpi.com/1424-8220/23/2/964*

869 Bogosian, D., Ferritto, J. & Shi, Y. (2002), Measuring uncertainty and conservatism in
870 simplified blast models, *in* '30th explosives safety seminar', Vol. 26, Department of
871 Defense Explosives Safety Board.

872 Chung Kim Yuen, S., Nurick, G. N., Langdon, G. S. & Iyer, Y. (2017), 'Deformation of
873 thin plates subjected to impulsive load: Part III – an update 25 years on', *International*
874 *Journal of Impact Engineering* **107**, 108–117.

875 Clarke, S. D., Fay, S. D., Warren, J. A., Tyas, A., Rigby, S. E. & Elgy, I. (2014), 'A large
876 scale experimental approach to the measurement of spatially and temporally localised
877 loading from the detonation of shallow-buried explosives', *Measurement Science and*
878 *Technology* **26**(1), 015001.
879 **URL:** *https://dx.doi.org/10.1088/0957-0233/26/1/015001*

880 Cloete, T. J. & Nurick, G. N. (2016), 'Blast characterization using a ballistic pendulum
881 with a centrally mounted hopkinson bar', *International Journal of Protective Structures*
882 **7**(3), 367–388.
883 **URL:** *https://doi.org/10.1177/2041419616663535*

884 Correlated Solutions (2024), *VIC-3D Software Manual*.

885 Curry, R. & Langdon, G. (2017), 'Transient response of steel plates subjected to close
886 proximity explosive detonations in air', *International Journal of Impact Engineering*
887 **102**, 102–116.

888 Curry, R., Langdon, G. & Tyas, A. (2025), Steel plates subjected to localised blast loading:
889 Transient measurements using ultra-high speed camera technology. Submitted to the
890 Journal of Strain.

891 Denefeld, V., Heider, N. & Holzwarth, A. (2017), 'Measurement of the spatial specific im-
892 pulse distribution due to buried high explosive charge detonation', *Defence Technology*
893 **13**, 219–227. SI: 30th International Symposium on Ballistics.
894 **URL:** *https://www.sciencedirect.com/science/article/pii/S2214914717300272*

895 Draganić, H., Varevac, D. & Lukić, S. (2018), 'An overview of methods for blast
896 load testing and devices for pressure measurement', *Advances in Civil Engineering*
897 **2018**(1), 3780482.
898 **URL:** *https://onlinelibrary.wiley.com/doi/abs/10.1155/2018/3780482*

899 Edwards, D, H., Thomas, G, O., Milne, A., Hooper, G. & Tasker, D. (1992), 'Blast wave
900 measurements close to explosive charges', *Shock Waves* **2**, 237–243.

901 Elveli, B. S., Vestrum, O., Hauge, K. O., Berstad, T., Børvik, T. & Aune, V. (2023),
902 'Thin steel plates exposed to combined ballistic impact and partially confined airblast

loading', *Engineering Failure Analysis* **144**, 106943.
URL: *https://www.sciencedirect.com/science/article/pii/S1350630722009104*

EPC Groupe (2022), *EURONEL 2 NON-ELECTRONIC DETONATORS*, EPC Groupe.

Farrimond, D. G., Rigby, S. E., Clarke, S. D. & Tyas, A. (2022), 'Time of arrival as a diagnostic for far-field high explosive blast waves', *International Journal of Protective Structures* **13**(2), 379–402.
URL: *https://doi.org/10.1177/20414196211062923*

Fourney, W. L., Leiste, U., Bonenberger, R. & and, D. J. G. (2005), 'Mechanism of loading on plates due to explosive detonation', *Fragblast* **9**(4), 205–217.

Fuller, B., Rigby, S., Tyas, A., Clarke, S., Warren, J., Reay, J., Gant, M. & Elgy, I. (2016), Experimentation and modelling of near field explosions, *in* 'Proceedings of the 24th Military Aspects of Blast and Shock', Halifax, Nova Scotia, Canada.

Hopkinson, B. (1914), 'A method of measuring the pressure produced in the detonation of high explosives or by the impact of bullets', *Proceedings of the Royal Society of London. Series A, Containing Papers of a Mathematical and Physical Character* **213**, 437–456.

Kaufmann, R., Olufsen, S. N., Fagerholt, E. & Aune, V. (2023), 'Reconstruction of surface pressures on flat plates impacted by blast waves using the virtual fields method', *International Journal of Impact Engineering* **171**, 104369.
URL: *https://www.sciencedirect.com/science/article/pii/S0734743X2200210X*

Kingery, C. N. & Bulmash, G. (1984), Airblast Parameters from TNT Spherical Air Burst and Hemispherical Surface Burst, Technical report, Defence Technical Information Center, Ballistic Research Laboratory, Aberdeen Proving Ground, Maryland, MD, USA.

Kujawińska, M., Malesa, M., Malowany, K., Piekarczuk, A., Tyminska-Widmer, L. & Targowski, P. (2011), 'Digital image correlation method: A versatile tool for engineering and art structures investigations', *Proceedings of SPIE - The International Society for Optical Engineering* **8011**, 330–.

Langdon, G., Lee, W. & Louca, L. (2015), 'The influence of material type on the response of plates to air-blast loading', *International Journal of Impact Engineering* **78**, 150–160.
URL: *https://www.sciencedirect.com/science/article/pii/S0734743X14003066*

Menkes, S. B. & Opat, H. J. (1973), 'Broken beams - Tearing and shear failures in explosively loaded clamped beams', *Experimental Mechanics* **13**(11), 480–486.

Nurick, G. N. & Martin, J. B. (1989), 'Deformation of thin plates subjected to impulsive loading-a review Part II: Experimental studies', *International Journal of Impact Engineering* **8**(2), 171–186.

Nurick, G. & Radford, A. (1997), 'Deformation and tearing of clamped circular plates subjected to localised central blast loads', *Recent developments in computational and applied mechanics: a volume in honour of John B. Martin* pp. 276–301.

Parks, V. (1980), 'The range of speckle metrology', *Experimental Mechanics* **20**, 181–191.

Pope, D. (2002), Response prediction of plate-reinforced concrete panels exposed to near-field blast, PhD thesis, University of Sheffield.

Qi, Z., Lin, Y., Liang, W., Liang, M., Chen, R. & Zhang, Y. (2024), 'Explosion power evaluation based on the energy absorption characteristics of expansion tube structure', *International Journal of Impact Engineering* **186**, 104886.
URL: *https://www.sciencedirect.com/science/article/pii/S0734743X24000113*

Quinn, M. K., Nunn, E., Adams, J., Tanner, M., Goulding, S., Cardy, A., Garrard, M., Stokes, N., Roberts, D. A. & Jewson, T. (2023), 'Application of pressure-sensitive paint for explosive blast measurements', *Measurement Science and Technology* **35**(3), 035201.
URL: *https://dx.doi.org/10.1088/1361-6501/ad0fd4*

Reu, P. L. & Miller, T. J. (2008), 'The application of high-speed digital image correlation', *The Journal of Strain Analysis for Engineering Design* **43**(8), 673–688.

Rigby, S. E., Akintaro, O. I., Fuller, B. J., Tyas, A., Curry, R. J., Langdon, G. S. & Pope, D. J. (2019b), 'Predicting the response of plates subjected to near-field explosions using an energy equivalent impulse', *International Journal of Impact Engineering* **128**, 24–36.

Rigby, S. E., Knighton, R., Clarke, S. D. & Tyas, A. (2020), 'Reflected Near-Field Blast Pressure Measurements Using High Speed Video', *Experimental Mechanics* **60**(7), 875–888.

Rigby, S. E., Tyas, A., Curry, R. J. & Langdon, G. S. (2019a), 'Experimental Measurement of Specific Impulse Distribution and Transient Deformation of Plates Subjected to Near-Field Explosive Blasts', *Experimental Mechanics* **59**(2), 163–178.

Shin, J., Whittaker, A. S. & Cormie, D. (2015), 'Incident and Normally Reflected Overpressure and Impulse for Detonations of Spherical High Explosives in Free Air', *Journal of Structural Engineering* **141**(12), 04015057.

Sutton, M., Cheng, M., Peters, W., Chao, Y. & McNeill, S. (1986), 'Application of an optimized digital correlation method to planar deformation analysis', *Image Vis Comput* **4**(3), 143–150.

969 Sutton, M., Wolters, W., Peters, W., Ranson, W. & McNeill, S. (1983), 'Determination of
970 displacements using an improved digital image correlation method', *Image Vis Comput*
971 **1**(3), 133–139.

972 Taylor, L., Fourney, W. & Leiste, H. (2010), 'Pressures on targets from buried explosions',
973 *Blasting Fragm* **4**, 165–192.

974 Tiwari, V., Sutton, M. A., McNeill, S., Xu, S., Deng, X., Fourney, W. L. & Bretall,
975 D. (2009), 'Application of 3d image correlation for full-field transient plate deforma-
976 tion measurements during blast loading', *International Journal of Impact Engineering*
977 **36**(6), 862–874.
978 **URL:** *https://www.sciencedirect.com/science/article/pii/S0734743X08002376*

979 Tyas, A. (2019), Blast loading from high explosive detonation: What we know and don't
980 know, *in* '13th International Conference on Shock and Impact Loads on Structures,
981 SILOS 2019', Guangzhou, China, pp. 13–15.

982 Tyas, A. & Pope, D. (2003), The energy take-up of panels subjected to near-field blast
983 loading, *in* 'Proc. of the XL 2003 Conf. on Response of Structures to Extreme Loading,
984 Toronto 2003', Toronto, Canada.

985 Wierzbicki, T. & Nurick, G. (1996), 'Large deformation of thin plates under localised
986 impulsive loading', *International journal of impact engineering* **18**(7), 899–918.